

Time-dependent multiconfiguration method applied to laser-driven H_2^+

Erik Lötstedt,^{*} Tsuyoshi Kato, and Kaoru Yamanouchi*Department of Chemistry, School of Science, The University of Tokyo, 7-3-1 Hongo, Bunkyo-ku, Tokyo 113-0033, Japan*

(Received 10 August 2018; revised manuscript received 12 October 2018; published 7 January 2019)

We apply the extended multiconfiguration time-dependent Hartree-Fock method to the simulation of a hydrogen molecular ion exposed to an intense laser pulse. By comparing the results obtained by this method with the results obtained by a method in which the time-dependent Schrödinger equation is solved directly on a three-dimensional grid, we find that the results obtained by these two methods are in good agreement with each other when the number of time-dependent expansion terms exceeds 8. We further compare the results with those obtained by the conventional two-state Born-Oppenheimer approximation. In order to interpret the resultant time-dependent wave functions, we decompose the total wave function into the natural electronic and protonic orbitals that diagonalize the single-particle density matrices and find that the pair of electronic and protonic natural orbitals carrying the largest population describes the vibrational excitation, while the pair carrying the second largest population describes the dissociation into $\text{H} + \text{H}^+$. We also examine the time-dependent motion of the protons in H_2^+ in terms of the time-dependent adiabatic potential-energy curves, which are defined as the instantaneous eigenvalues of the Hamiltonian matrix governing the time-dependent motion of the protonic orbitals. We show that two potential minima are formed on the lowest-energy adiabatic potential-energy curve and that the nuclear wave packet localized in the inner minimum corresponds to the bound vibrational motion, while the nuclear wave packet localized in the outer minimum corresponds to the dissociation.

DOI: [10.1103/PhysRevA.99.013404](https://doi.org/10.1103/PhysRevA.99.013404)

I. INTRODUCTION

When a molecule containing hydrogen atoms is exposed to an intense laser pulse, the hydrogen atoms within the molecule have been known to move very fast, as has been demonstrated experimentally for methanol [1,2]. It was shown that the time scale of the hydrogen migration process, $\text{CH}_3\text{OH}^+ \rightarrow \text{CH}_2\text{OH}_2^+$, can be estimated to be about 25 fs. For acetylene, it was also shown experimentally that the isomerization reaction, $\text{HCCH}^+ \rightarrow \text{CCH}_2^+$, proceeds within 50 fs [3–5].

In order to describe theoretically these ultrafast processes in which responses of electrons to the external laser field trigger the subsequent motion of protons or hydrogen atoms, a method that can treat the time-dependent motion of electrons and protons on an equal footing is required. In the conventional Born-Oppenheimer (BO) treatment of light-molecule interaction, we represent the total wave function Ψ^{BO} as [6]

$$\Psi^{\text{BO}}(\mathbf{r}, \mathbf{R}, t) = \sum_{j=1}^K \chi_j^{\text{BO}}(\mathbf{R}, t) \phi_j^{\text{BO}}(\mathbf{r}; \mathbf{R}), \quad (1)$$

where \mathbf{r} is a collective coordinate of all the electrons, \mathbf{R} is a collective coordinate of all the nuclei, $\phi_j^{\text{BO}}(\mathbf{r}; \mathbf{R})$ is the wave function of the adiabatic electronic state j , depending parametrically on \mathbf{R} , $\chi_j^{\text{BO}}(\mathbf{R}, t)$ is the nuclear wave function in the state j , and K is an integer defining the length of the expansion. Even though Eq. (1) is exact in the limit of a complete set of the electronic states ϕ_j^{BO} , we have to truncate the sum over j to at most a few bound electronic states for

practical reasons. In this case, because no electronic continuum states are included in the expansion in Eq. (1), we could not describe hydrogen migration occurring simultaneously with the ionization. Another drawback of the ansatz (1) is that it requires the set $\{\phi_j^{\text{BO}}(\mathbf{r}; \mathbf{R})\}$ to be calculated and stored for each value of the collective nuclear coordinate \mathbf{R} . For a nonlinear polyatomic molecule containing N atoms, the number of the vibrational degrees of freedom is $3N - 6$, leading to the $(3N - 6)$ -dimensional potential-energy surface. Even for a tetratomic molecule ($N = 4$), it is not practical to calculate the electronic states and the potential-energy surface at each value of \mathbf{R} because the number of dimensions is too large. For this reason, time-dependent simulations of polyatomic molecules in intense laser fields including electronic excitation is limited to small-sized molecules such as H_2^+ [7–21], H_3^{2+} [22,23], O_3 [24], NO_2 [25,26], LiF [27], or HeH_2^+ [28]. There are other approaches such as the direct dynamics variational multiconfiguration Gaussian method [29–31] that are based on the BO approximation. These methods can only be applicable when we evaluate the potential-energy surfaces by avoiding the calculation of global potential-energy surfaces.

An alternative ansatz for the total wave function is [32]

$$\Psi(\mathbf{r}, \mathbf{R}_N, t) = \sum_{j=1}^{K_p} \sum_{k=1}^{K_e} C_{jk}(t) \chi_j(\mathbf{R}_N, t) \phi_k(\mathbf{r}, t), \quad (2)$$

where \mathbf{R}_N is a collective coordinate for all nuclei, $\chi_j(\mathbf{R}_N, t)$ is a nuclear wave function, $\phi_k(\mathbf{r}, t)$ is an electronic wave function, $C_{jk}(t)$ is an expansion coefficient, and the integers K_p and K_e specify the number of expansion terms. Because of Löwdin's expansion theorem [33], we expect that the exact wave function can be constructed in the limit of large

^{*}lotstedt@chem.s.u-tokyo.ac.jp

K_p and K_e . The method based on the ansatz (2) is called the multiconfiguration electron-nuclear dynamics (MCEND) method [32].

A similar wave function ansatz, which stresses the fermionic nature of the protons, is [34]

$$\Psi(\mathbf{r}, \mathbf{R}_p, \mathbf{R}_n, t) = \sum_{j=1}^{K_p} \sum_{k=1}^{K_e} C_{jk}(\mathbf{R}_n, t) \chi_j(\mathbf{R}_p, t) \phi_k(\mathbf{r}, t), \quad (3)$$

where \mathbf{R}_p is a collective coordinate for all the protons in the molecule, $\chi_j(\mathbf{R}_p, t)$ is a protonic wave function, \mathbf{R}_n is a collective coordinate for all other nuclei, and $C_{jk}(\mathbf{R}_n, t)$ is an \mathbf{R}_n -dependent expansion coefficient. This approach, pioneered in Ref. [34], is referred to as the extended multiconfiguration time-dependent Hartree-Fock (Ex-MCTDHF) method, because it extends the MCTDHF method [35–37] developed for electrons so that the protonic motion is included on the same level of approximation as the electronic motion. In Ref. [34], it was stressed that the protonic part of the wave function needs to be antisymmetric under the exchange of two protons because of their fermionic nature. In both the MCEND method and the Ex-MCTDHF method, the nuclear degrees of freedom are treated on the same footing as the electronic degrees of freedom.

The basic idea of the wave functions in Eqs. (2) and (3) that the different degrees of freedom are described using different sets of time-dependent basis functions was introduced earlier in the multiconfiguration time-dependent Hartree (MCTDH) method [38–42]. The MCTDH method, originally developed for calculating vibrational wave functions, was extended first to the description of systems composed of electrons and has been called the MCTDHF method [35–37], and then, to the description of systems composed of bosonic particles, and has been referred to as the MCTDHB method [43–45]. Recently, the MCTDH method was extended so that it can treat mixtures of two different fermionic species [46,47]. Therefore, this extended theory [46,47] can also be applied to a system composed of electrons and protons.

There are two noteworthy features in Eqs. (2) and (3). First, the electronic wave function $\phi_k(\mathbf{r}, t)$ depends on time t . This allows us to describe the electronic excitation in a very flexible manner because $\phi_k(\mathbf{r}, t)$ no longer represents a particular electronic state. Therefore, the MCEND and Ex-MCTDHF methods can describe, in principle, any motion of electrons and nuclei, such as simultaneous ionization and dissociation. Second, the electronic wave functions $\phi_k(\mathbf{r}, t)$ do not depend on the nuclear coordinates \mathbf{R} . This is in contrast to the Born-Oppenheimer approximation (1) in which the electronic wave functions $\phi_j^{\text{BO}}(\mathbf{r}; \mathbf{R})$ depend on \mathbf{R} by construction.

The Ex-MCTDHF method has been successfully applied to H_2 in Ref. [48] and to CH_3OH in Ref. [49] and the time-independent electroprotonic wave functions were obtained. However, the Ex-MCTDHF method has not yet been shown to work efficiently for deriving time-dependent wave functions. The MCEND method was adopted for calculating the bound electron motion and nondissociative nuclear motion of a LiH molecule [50]. In Ref. [51], the MCTDHF method was extended so that the vibrational motion in diatomic molecules can be treated using an electronic basis set depending on the internuclear distance and was tested for

single-photon ionization [52]. Therefore, it is worthwhile to examine whether the Ex-MCTDHF method can be applied to time-dependent strong-field processes involving simultaneous motions of electrons and nuclei. In particular, we aim to confirm that the wave function described by the ansatz Eq. (3) can correctly model molecular dissociation, where electrons and nuclei have a strong spatial correlation. In the BO ansatz (1), this spatial correlation is automatically included because of the \mathbf{R} dependence of the electronic states, but it is not obvious if the Ex-MCTDHF method could describe correctly the behavior of the total wave function at dissociation because both the nuclear wave functions and the electronic wave functions are required to be changed largely in the course of the dissociation.

In this paper, we apply the Ex-MCTDHF method to simulate the strong-field ionization and dissociation of H_2^+ . Because H_2^+ contains only one electron, the electronic wave functions $\phi_k(\mathbf{r}, t)$ in Eq. (3) are single-electron orbitals and the protonic wave functions $\chi_j(\mathbf{R}_p, t)$ are protonic orbitals defined as a function of the internuclear distance $\mathbf{R}_p = R$. Because neither the electronic part nor the protonic part of the wave function needs to be antisymmetrized, the Ex-MCTDHF wave function of H_2^+ is equivalent to an MCTDH wave function [38–42,53] as long as the two degrees of freedom of an electron are treated by the mode combination [54,55]. A model of H_2^+ exposed to an intense laser pulse in which the motion of the electron was restricted to one dimension was investigated in Ref. [53], but the correlation among the electron and the two protons during dissociation was not explicitly discussed. For larger molecules than H_2^+ having several electrons and protons, we have to use the Ex-MCTDHF method in which both the protonic and the electronic parts of the wave function are antisymmetrized. Because H_2^+ is the simplest system that can be described by the ansatz (3), we examine the performance of the Ex-MCTDHF method on the description of H_2^+ interacting with an intense laser pulse as the starting point for its further applications to many-electron polyatomic molecules.

We show that the Ex-MCTDHF method can describe simultaneously ionization, dissociation, and vibrational excitation of H_2^+ induced by an intense laser pulse. By comparing the results obtained by the Ex-MCTDHF method with those obtained by a direct grid method serving as a reference, we investigate the convergence properties of the Ex-MCTDHF wave function with the number of configurations K . We also compare the Ex-MCTDHF results with those obtained using the standard BO approximation.

In order to analyze the properties of the time-dependent wave functions varying as a function of both electronic and nuclear coordinates, we introduce two methods. In the first method, we decompose the total wave function into the protonic and electronic orbitals that diagonalize the respective single-particle density matrices and show that the two pairs of protonic and electronic natural orbitals having the largest populations are assigned to the respective different dynamical channels, that is, one pair corresponds to the dissociation and the other corresponds to the vibrational excitation. In the second method, we define time-dependent potential-energy curves for a time-dependent electronuclear wave function by diagonalizing the time-dependent Hamiltonian matrix

governing the nuclear motion, in a manner suggested in Ref. [56]. On the basis of these time-dependent potential-energy curves, we investigate the laser-induced dissociation dynamics of H_2^+ and show that dissociation may be interpreted as a vibrational wave packet moving on a time-dependent potential well.

II. THEORY

We consider a model system of H_2^+ , in which two protons are placed on the z axis and the position of an electron measured from the center of mass of the two protons (Jacobian coordinates [57]) is represented by the cylindrical coordinate system (z, ρ, φ) . We neglect the rotational motion of the system and assume that the laser polarization direction is parallel to the z axis. We also assume that the electronic wave function has σ symmetry, so that it has no dependence on the azimuthal angle φ . The total Hamiltonian is given in the center-of-mass frame by

$$H(t) = h_e(z, \rho, t) + h_p(R) + U(z, \rho, R), \quad (4)$$

where

$$h_e(z, \rho, t) = -\frac{\hbar^2}{2\mu_e} \left[\frac{1}{\rho} \frac{\partial}{\partial \rho} \left(\rho \frac{\partial}{\partial \rho} \right) + \frac{\partial^2}{\partial z^2} \right] + eE(t)vz \quad (5)$$

is the electronic part of the Hamiltonian,

$$h_p(R) = -\frac{\hbar^2}{2\mu_p} \frac{1}{R^2} \frac{\partial}{\partial R} \left(R^2 \frac{\partial}{\partial R} \right) + \frac{e^2}{R} \quad (6)$$

is the protonic part of the Hamiltonian, and

$$U(z, \rho, R) = \frac{-e^2}{\sqrt{(z - \frac{R}{2})^2 + \rho^2}} + \frac{-e^2}{\sqrt{(z + \frac{R}{2})^2 + \rho^2}} \quad (7)$$

is the attractive Coulomb interaction potential. In Eqs. (5) and (6), $\mu_e = 2Mm_e/(2M + m_e)$ is the reduced electron mass, $v = 1 + m_e/(2M + m_e)$, and $\mu_p = M/2$, where m_e is the electron mass and $M \approx 1836.15m_e$ is the mass of the proton [58]. We note that there is no mass polarization term in the Hamiltonian for a one-electron system, but the effect of the separation of the relative coordinates and the center-of-mass coordinate appears in the reduced electron mass μ_e . Because H_2^+ is a homonuclear molecule, there is no term representing the dipole coupling with the laser field in the protonic Hamiltonian (6).

The laser field $E(t)$ in Eq. (5) is expressed by the following form:

$$E(t) = \begin{cases} E_0 \sin(\omega_0 t) \sin^2\left(\frac{\pi t}{T_0}\right) & \text{when } 0 \leq t \leq T_0, \\ 0 & \text{otherwise,} \end{cases} \quad (8)$$

where E_0 is the peak value of the electric field, ω_0 is the angular frequency of the laser pulse, $T_0 = 2\pi n_c/\omega_0$ is the total pulse width, and n_c is the number of the optical cycles. The relation between T_0 and the full width at half maximum T_{FWHM} of the intensity envelope is $T_{\text{FWHM}} \approx 0.36T_0$.

The time-dependent Schrödinger equation (TDSE) for the total wave function $\Psi(\rho, z, R, t)$ reads

$$i\hbar \frac{\partial \Psi(\rho, z, R, t)}{\partial t} = H(t)\Psi(\rho, z, R, t). \quad (9)$$

A. Ex-MCTDHF

In the Ex-MCTDHF method, the total wave function is written as

$$\Psi(z, \rho, R, t) = \sum_{j,k=1}^K C_{jk}(t) \phi_j(z, \rho, t) \chi_k(R, t), \quad (10)$$

where K is an integer defining the length of the expansion. Hereafter, we refer to the ϕ_j 's as electronic orbitals, and the χ_k 's as protonic orbitals. In the case of a single-electron system, we should use the same number K for the protonic and electronic orbitals [40]. The wave function (10) has the same form as Eq. (3), if we identify \mathbf{r} with (z, ρ) , \mathbf{R}_p with the internuclear distance R , and set K_p and K_e to be $K_p = K_e = K$. The time-dependent coefficients $C_{jk}(t)$ do not depend on the nuclear coordinates because there are no nuclei other than the two protons, and all the electronic orbitals $\phi_j(z, \rho, t)$ do not depend on the azimuthal angle φ because the total wave function does not depend on φ .

By applying the time-dependent variational principle [59–61] $\langle \delta \Psi | H - i\hbar \frac{\partial}{\partial t} | \Psi \rangle = 0$, we derive the equations of motion [34,40],

$$i\hbar \frac{\partial \phi_j(z, \rho, t)}{\partial t} = Q^e \left(h_e(z, \rho, t) \phi_j(z, \rho, t) + \sum_{k,l,m,n=1}^K D_{jk}^{e-1} C_{km}^* C_{ln} U_{mn}^e \phi_l(z, \rho, t) \right) \quad (11)$$

for the electronic orbitals,

$$i\hbar \frac{\partial \chi_j(R, t)}{\partial t} = Q^p \left(h_p(R) \chi_j(R, t) + \sum_{k,l,m,n=1}^K D_{jk}^{p-1} C_{mk}^* C_{nl} U_{mn}^p \chi_l(R, t) \right) \quad (12)$$

for the protonic orbitals, and

$$i\hbar \frac{dC_{jk}}{dt} = \sum_{l,m=1}^K \langle \phi_j \chi_k | H(t) | \phi_l \chi_m \rangle C_{lm}(t) \quad (13)$$

for the coefficients $C_{jk}(t)$. In Eqs. (11) and (12), we use the density matrices $D_{jk}^{e,p}$ defined as

$$D_{jk}^e = \sum_{l=1}^K C_{jl}^* C_{kl}, \quad (14)$$

$$D_{jk}^p = \sum_{l=1}^K C_{lj}^* C_{lk}, \quad (15)$$

and the mean-field potentials

$$U_{jk}^e(z, \rho, t) = \int R^2 dR \chi_j^*(R, t) \chi_k(R, t) U(z, \rho, R), \quad (16)$$

$$U_{jk}^p(R, t) = \int \rho d\rho dz \phi_j^*(z, \rho, t) \phi_k(z, \rho, t) U(z, \rho, R). \quad (17)$$

The symbols $Q^{e,p}$ appearing in Eqs. (11) and (12) represent the projection operators whose actions are defined as

$$Q^e f(z, \rho) = f(z, \rho) - \sum_{j=1}^K \phi_j(z, \rho) \langle \phi_j | f \rangle \quad (18)$$

and

$$Q^p g(R) = g(R) - \sum_{j=1}^K \chi_j(R) \langle \chi_j | g \rangle \quad (19)$$

for arbitrary functions $f(z, \rho)$ and $g(R)$. The projection operators $Q^{e,p}$ guarantee that the orbitals are orthonormal at all times, that is,

$$\langle \phi_j(t) | \phi_k(t) \rangle = \delta_{jk} \quad (20)$$

and

$$\langle \chi_j(t) | \chi_k(t) \rangle = \delta_{jk}, \quad (21)$$

provided that the orbitals are orthonormal at $t = 0$.

The coefficients $C_{jk}(t)$ are normalized at all times as

$$\sum_{j,k=1}^K C_{jk}^*(t) C_{jk}(t) = 1, \quad (22)$$

which, together with Eqs. (20) and (21), means that $\int R^2 dR \rho d\rho dz |\Psi(z, \rho, R, t)|^2 = 1$.

B. Two-state BO model

The two-state BO model of H_2^+ in which the two lowest adiabatic BO electronic states are included in the expansion of the wave function can be called the ‘‘standard’’ model of laser-driven H_2^+ . The total wave function is written as

$$\Psi^{\text{BO}}(z, \rho, R, t) = \sum_{j=1}^2 \phi_j^{\text{BO}}(z, \rho; R) \chi_j^{\text{BO}}(R, t), \quad (23)$$

where a superscript BO is attached to discriminate the orbitals from the Ex-MCTDHF orbitals in Eq. (10).

This two-state BO model has often been employed in theoretical studies on the strong-field dissociation of H_2^+ [9,10,15,62]. In particular, the two-state BO model has been used for the interpretation [12,20,21] of the experimental results on the asymmetric proton ejection in the laser-induced dissociation, $H_2^+ \rightarrow H + H^+$ [13,16,17], where the ratio between the number of protons ejected along the direction parallel to the laser polarization direction and the number of protons ejected along the antiparallel direction varies as a function of the carrier-envelope phase of the laser pulse.

In Eq. (23), it is assumed that the BO electronic states satisfy

$$[h_e(z, \rho, 0) + U(z, \rho, R)] \phi_j^{\text{BO}}(z, \rho; R) = \epsilon_j(R) \phi_j^{\text{BO}}(z, \rho; R) \quad (24)$$

at each value of R . The operators h_e and U were defined in Eqs. (5) and (7), respectively. The states $\phi_j^{\text{BO}}(z, \rho; R)$ ($j = 1, 2$) included in the expansion (23) are the two states having the lowest energy $\epsilon_j(R)$, the $1s\sigma_g$ ($j = 1$) and $2p\sigma_u$ ($j = 2$) states, with which the dissociation of H_2^+ is described.

Inserting the ansatz (23) into the time-dependent Schrödinger equation (9), and neglecting the terms containing $\partial \phi_j^{\text{BO}} / \partial R$, which corresponds to the BO approximation, we obtain the coupled equations of motion for the two protonic orbitals,

$$i\hbar \frac{\partial \chi_j^{\text{BO}}(R, t)}{\partial t} = [h_p(R) + \epsilon_j(R)] \chi_j^{\text{BO}}(R, t) + eE(t)v \sum_{\substack{k=1s\sigma_g, \\ 2p\sigma_u}} \langle \phi_j^{\text{BO}} | z | \phi_k^{\text{BO}} \rangle \chi_k^{\text{BO}}(R, t). \quad (25)$$

We note that in the two-state BO approximation, the nonadiabatic transition matrix element $\langle \phi_{1s\sigma_g}^{\text{BO}} | \partial \phi_{2p\sigma_u}^{\text{BO}} / \partial R \rangle$ vanishes identically because of the different symmetry of the $1s\sigma_g$ and $2p\sigma_u$ states.

III. RESULTS

In this section, we compare the results of simulations performed by the following three different methods: the Ex-MCTDHF method, the direct method by which the time-dependent Schrödinger equation is numerically solved without making a product expansion, and the two-state BO method. In all the three methods, a grid-type discretization for the three degrees of freedom (ρ , z , and R) is adopted. The direct method is referred to hereafter as the three-dimensional (3D)-grid method. The details of the numerical methods employed can be found in Appendix. The grid parameters, that is, the number of grid points and the mesh widths for the respective degrees of freedom, are set to be the same in the calculations performed by these three methods.

A. Ground state

Before investigating the time-dependent dynamics, we need to compute the vibronic ground state of H_2^+ . In the Ex-MCTDHF method as well as in the direct 3D-grid method, the imaginary time propagation method is used for finding the ground state. We solve Eqs. (11)–(13) (in the case of Ex-MCTDHF) and Eq. (9) (in the case of the direct 3D-grid method) with the substitution $t \rightarrow -it$, starting from an appropriate initial guess. In the two-state BO model, the ground state is obtained by the diagonalization of the grid representation of the Hamiltonian.

The ground-state energies ϵ_0 obtained by the three different methods are shown in Fig. 1. We can see that the ground-state energy obtained by the Ex-MCTDHF method converges to the ground-state energy obtained by the direct 3D-grid method at $K = 4$. We have $\epsilon_0^{\text{(Ex-MCTDHF)}}(K = 4) = -0.58497E_h$, $\epsilon_0^{\text{(Ex-MCTDHF)}}(K \geq 6) = -0.58499E_h$, and $\epsilon_0^{\text{(3D-grid)}} = -0.58500E_h$, where $E_h \approx 27.21$ eV denotes one hartree. The accurate value for the nonrelativistic energy of the rovibronic ground state of H_2^+ , obtained by the specially adapted basis sets [63,64] or by the free complement method [65], is $\epsilon_0^{\text{(exact)}} = -0.59714E_h$ [63–65], which can be used as a reference value. The difference between $\epsilon_0^{\text{(Ex-MCTDHF)}}(K = 12)$ and $\epsilon_0^{\text{(exact)}}$ is $\epsilon_0^{\text{(Ex-MCTDHF)}}(K = 12) - \epsilon_0^{\text{(exact)}} \approx 0.01E_h$, and can be ascribed to the fact

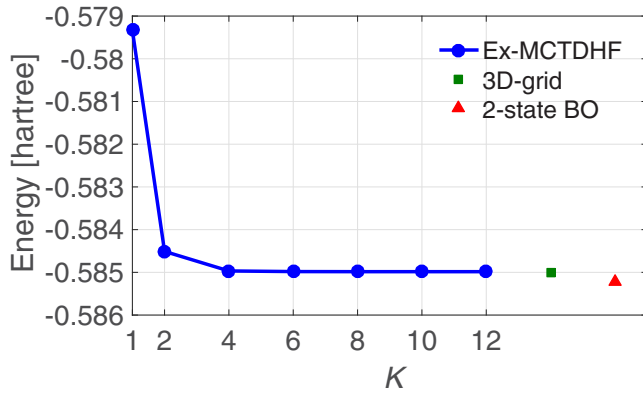


FIG. 1. Ground-state energies ε_0 of H_2^+ obtained by the three different methods: Ex-MCTDHF, the direct 3D-grid method, and the two-state BO method. In the Ex-MCTDHF case, the ground-state energy is shown as a function of the expansion length parameter K , representing the total number of terms included in the Ex-MCTDHF expansion as defined in Eq. (10).

that the numerical grid employed in the present study is not sufficiently fine for reproducing the exact ground-state energy. The grid spacings employed in the present study, $\Delta z = \Delta \rho = \Delta R = 0.1a_0$ ($a_0 \approx 0.53 \text{ \AA}$ is the Bohr radius), were chosen so that the computational time needed for the time-dependent simulations falls in an affordable range. We have confirmed that $\varepsilon_0^{\text{(Ex-MCTDHF)}}(K=12) = -0.59683E_h$ and $\varepsilon_0^{\text{(3D-grid)}} = -0.59683E_h$ are obtained by decreasing the mesh width to $\Delta z = \Delta \rho = \Delta R = 0.0125a_0 \approx 0.0066 \text{ \AA}$, showing that both the Ex-MCTDHF method and the 3D-grid method reproduce the accurate ground-state energy reported in Refs. [63–65] if the mesh width is sufficiently small.

We obtain the ground-state energy $\varepsilon_0^{\text{BO}}$ of the two-state BO method shown in Fig. 1 by solving the vibrational eigenvalue equation for the electronic ground $1s\sigma_g$ state,

$$[h_p(R) + \epsilon_{1s\sigma_g}(R)]\chi_0^{\text{BO}}(R) = \varepsilon_0^{\text{BO}}\chi_0^{\text{BO}}(R), \quad (26)$$

which is the time-independent equivalent of Eq. (25). As can be seen in Fig. 1, the resulting energy $\varepsilon_0^{\text{BO}}$ is lower than $\varepsilon_0^{\text{(3D-grid)}}$ by approximately $2 \times 10^{-4}E_h$. Because the BO ground-state energy $\varepsilon_0^{\text{BO}}$ is obtained by solving Eq. (26) having no nonadiabatic corrections in the Hamiltonian, $\varepsilon_0^{\text{BO}}$ can be lower than $\varepsilon_0^{\text{(3D-grid)}}$, even though the same numerical grid is adopted in both methods. If we use the full 3D-grid Hamiltonian for evaluating the energy of the BO ground-state wave function, we obtain $\langle \phi_{1s\sigma_g}^{\text{BO}}\chi_0^{\text{BO}} | H(0) | \phi_{1s\sigma_g}^{\text{BO}}\chi_0^{\text{BO}} \rangle = -0.585003E_h$, which is in good agreement with $\varepsilon_0^{\text{(3D-grid)}} = -0.585004E_h$. This shows that the BO ground-state wave function is an accurate approximation of the exact wave function, and that the difference between the BO ground-state energy and the exact ground-state energy originates from the omission of the nonadiabatic correction terms in the BO Hamiltonian. As a further confirmation of the validity of the BO ground-state wave function, we have checked that the zero-point energy $\varepsilon_0^{\text{BO}} - \epsilon_{1s\sigma_g}(R_{\text{eq}}) \approx 5.0 \times 10^{-3}E_h$ at the equilibrium internuclear distance $R_{\text{eq}} \approx 1.06 \text{ \AA}$ agrees with the more accurate BO calculations presented

in Ref. [66], where a value of $5.2 \times 10^{-3}E_h$ was obtained for the zero-point energy. By decreasing the mesh width to $\Delta R = 0.0125a_0$ we obtain $\varepsilon_0^{\text{(BO)}} = -0.59705E_h$, which is in agreement with the value $\varepsilon_0^{\text{(exact)}} = -0.59714E_h$ obtained in Refs. [63–65].

B. Time-dependent dynamics

In this section, we report on the results of a simulation of H_2^+ exposed to an intense laser pulse. The laser field is assumed to have the form shown in Eq. (8). In all the simulations presented below we take the laser parameters of $E_0 = 0.119e/a_0^2 \approx 61 \text{ GV/m}$ corresponding to the peak intensity of $5 \times 10^{14} \text{ W/cm}^2$, $\omega_0 = 0.114E_h/\hbar \approx 4.7 \text{ fs}^{-1}$ corresponding to the wavelength of 400 nm, and $n_c = 10$ corresponding to the pulse width of $T_0 = 13 \text{ fs}$, where the pulse width is defined as the entire time interval where the laser pulse is nonvanishing.

In each of the three methods we set the initial wave function $\Psi(z, \rho, R, t=0)$ to be the ground-state wave function. An absorbing boundary is used to absorb the electronic density reaching the boundary of the computational domain. Details of the numerical methods employed in the present study can be found in Appendix.

We discuss first the time-dependent dynamics by showing the protonic density $P(R, t)$, which is defined as the total wave function squared integrated over the electronic coordinates,

$$P(R, t) = R^2 \int \rho d\rho dz |\Psi(\rho, z, R, t)|^2. \quad (27)$$

The resultant protonic densities $P(R, t)$ are shown in Fig. 2. The results obtained by the Ex-MCTDHF method are shown for six K values ($K = 1, 2, 4, 8, 10$, and 12). In all the cases except for Ex-MCTDHF with $K = 1$, a bifurcation into two components occurs after the laser pulse vanishes at $t \approx 13 \text{ fs}$; one component whose average internuclear distance $\langle R \rangle$, defined as $\langle R \rangle = \int dR P(R, t)R$, increases with time, representing dissociation and the other component whose $\langle R \rangle$ oscillates and remains in the bound domain, representing a vibrational wave packet oscillating in the bound well.

By comparing the Ex-MCTDHF results and the direct 3D-grid result in Fig. 2, we can see that the protonic density obtained by the Ex-MCTDHF method becomes closer to the protonic density obtained by the direct 3D-grid method as K increases, as expected. Therefore, the result obtained by the direct 3D-grid method can be regarded as a reference to which the results obtained by the Ex-MCTDHF method could converge when K becomes larger. A K -convergence rate similar to the one shown here was reported before in Refs. [53,67,68], where a method equivalent to Ex-MCTDHF was used to simulate laser-driven H_2^+ . The major difference between the simulations presented in Refs. [53,67,68] and our simulation is in the dimensionality of the motion of an electron. In Refs. [53,67,68], an electron was restricted to move along the z axis in one dimension, while, in the present study, an electron can move in the two-dimensional cylindrical space, that is, the three-dimensional space whose dimension is reduced by one by the cylindrical symmetry. Similarly to Refs. [53,67,68], we find that $K = 8$ is required for the

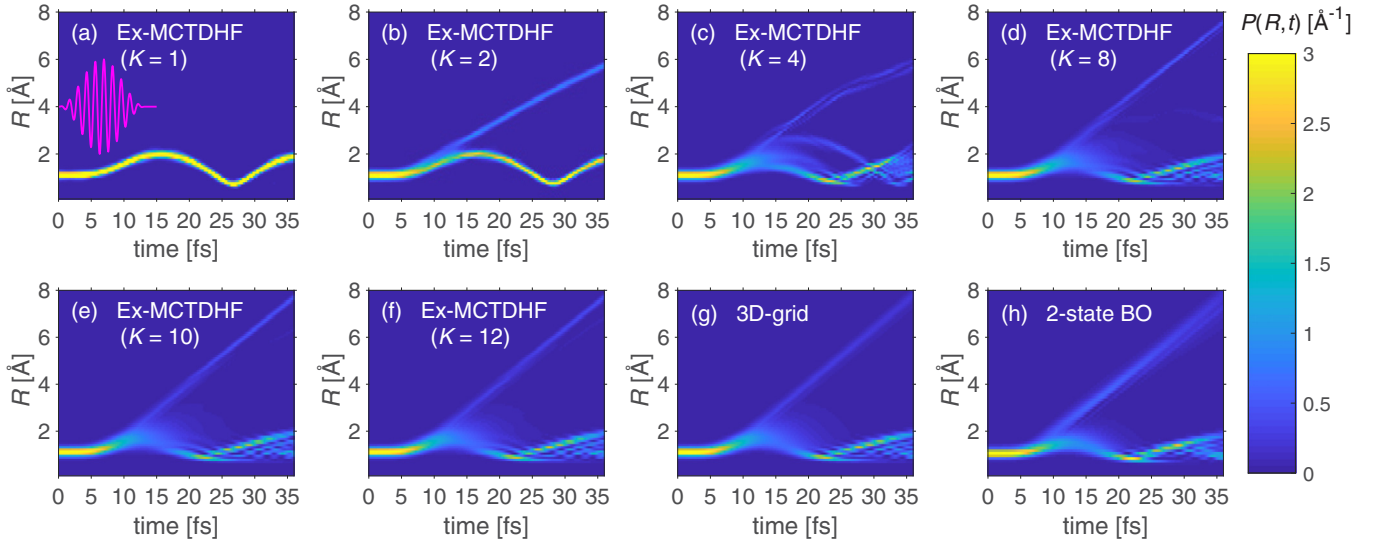


FIG. 2. Time-dependent protonic density $P(R, t)$ [see Eq. (27) for the definition] for the laser field with the peak intensity of $5 \times 10^{14} \text{ W/cm}^2$ and the wavelength of 400 nm. The total pulse width is $T_0 = 13$ fs, which means that the electric field vanishes when $t > 13$ fs. Panels (a)–(f) display the results of the simulation using the Ex-MCTDHF method with different values of the expansion length parameter K . Panel (g) shows the result of the simulation using the direct 3D-grid method, and (h) shows the result of the two-state BO model defined by Eq. (25). The temporal variation of the laser field is shown in (a).

Ex-MCTDHF results in order to have a sufficiently good agreement with the direct 3D-grid results. We also remark that $K = 2$ is large enough to reproduce the bifurcation into the bound component and the dissociating component.

In Fig. 2(h), we show $P(R, t)$ obtained by the two-state BO method. Even though the ionization and excitation to the higher-lying excited states are excluded in this model, the protonic density $P(R, t)$ still shows a reasonably good agreement with the result obtained by the direct 3D-grid method shown in Fig. 2(g).

In order to discuss the differences in the protonic densities shown in Fig. 2 more precisely, we show in Fig. 3 the protonic densities at $t = 36$ fs, the longest propagation time in the simulation. As shown in Fig. 3, the result obtained by the Ex-MCTDHF($K = 12$) exhibits a certain deviation from the result obtained by the direct 3D-grid method. For example, the peak at around 7.7 \AA is narrower in the Ex-MCTDHF($K = 12$) result than in the direct 3D-grid result, and there is a small peak at $R \approx 6.7 \text{ \AA}$ appearing in the Ex-MCTDHF($K = 12$) distribution, which is absent in the 3D-grid distribution.

As can be seen in Fig. 3, a part of the protonic density representing the dissociation obtained by the Ex-MCTDHF($K = 4$) method is incorrectly centered at around $R \approx 5.7 \text{ \AA}$ which is shorter by about 2 \AA than $R \approx 7.7 \text{ \AA}$. On the other hand, in the two-state BO method the protonic density $P(R, 36 \text{ fs})$ exhibits a peak at $R \approx 7.7 \text{ \AA}$. Therefore, it can be said that the two-state BO method gives closer results to the direct 3D-grid result than the Ex-MCTDHF($K = 4$) method. At $K = 12$, the Ex-MCTDHF result becomes closer to the direct 3D-grid result than the two-state BO result. Indeed, the peak at $R \approx 7.7 \text{ \AA}$ obtained by the two-state BO method is too broad compared with the direct 3D-grid result, and the amplitude of the peak in the vibrational wave packet at around 1 \AA is too large. We conclude that the protonic density $P(R, t)$ produced after the laser-molecule interaction is represented

better by the Ex-MCTDHF method than by the two-state BO method as long as $K \gtrsim 10$.

The Ex-MCTDHF method has an advantage over the two-state BO method because the Ex-MCTDHF method can handle both electronic excitation to the higher-lying states and ionization, which are excluded in the two-state BO method. The total probability of ionization $p_{\text{ion}}(t)$ can be estimated by

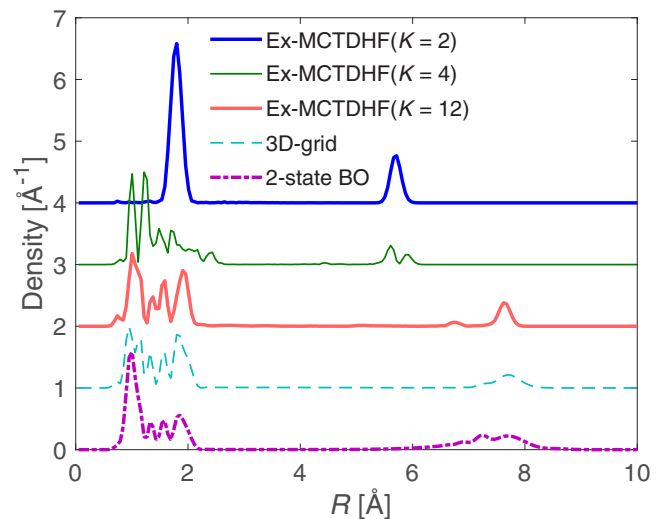


FIG. 3. Protonic densities $P(R, t_f)$ at $t_f = 36$ fs. The results obtained by the Ex-MCTDHF method using the three different values of K are compared with the result obtained by the 3D-grid method and that obtained by the two-state BO method. The laser parameters adopted here are the same as in Fig. 2. For better visibility, the Ex-MCTDHF curves were vertically shifted by $+4 \text{ \AA}^{-1}$ ($K = 2$), $+3 \text{ \AA}^{-1}$ ($K = 4$), and $+2 \text{ \AA}^{-1}$ ($K = 12$). The 3D-grid curve was shifted vertically by $+1 \text{ \AA}^{-1}$.

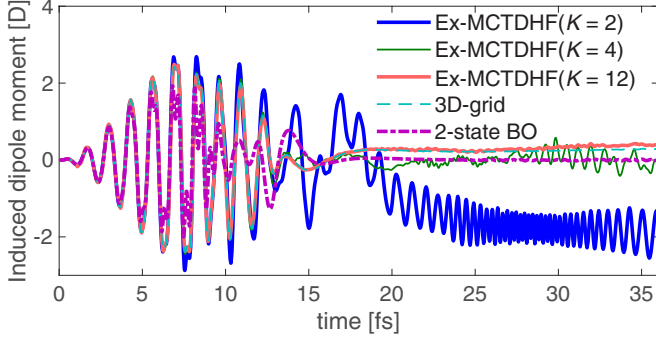


FIG. 4. Induced dipole moment $d(t)$ defined by Eq. (29). The laser parameters are the same as those adopted in Fig. 2: the peak intensity is 5×10^{14} W/cm², the wavelength is 400 nm, and the total pulse width is $T_0 = 13$ fs. In the time range of $0 \leq t \leq 15$ fs, the Ex-MCTDHF ($K = 12$) curve and the 3D-grid curve overlap almost completely.

the decrease in the total norm of the wave function on the computational grid,

$$p_{\text{ion}}(t) = 1 - \int_0^{\rho_{\text{max}}} \rho d\rho \int_{-z_{\text{max}}}^{z_{\text{max}}} dz \int_0^{R_{\text{max}}} R^2 dR \times |\Psi(\rho, z, R, t)|^2, \quad (28)$$

as long as the dissociative components of the wave function do not reach the grid boundary at time t . As shown in Figs. 2 and 3, at $t = 36$ fs, the dissociating component stays in the molecular domain and does not reach the grid boundary located at $R_{\text{max}} = 13$ Å. The ionization probabilities at $t = 36$ fs evaluated by Eq. (28) are $p_{\text{ion}}^{(\text{Ex-MCTDHF})}(t = 36 \text{ fs}) \approx 0.07$ for $K = 1$, $p_{\text{ion}}^{(\text{Ex-MCTDHF})}(36 \text{ fs}) \approx 0.16$ for $K = 2$, $p_{\text{ion}}^{(\text{Ex-MCTDHF})}(36 \text{ fs}) \approx 0.17$ for $K = 4, 8, 10, 12$, and $p_{\text{ion}}^{(3\text{D-grid})}(t = 36 \text{ fs}) \approx 0.17$, showing that the ionization probability obtained by the Ex-MCTDHF method with $K \geq 2$ agrees well with that obtained by the 3D-grid method.

Another physical property for which the Ex-MCTDHF method gives better results than the two-state BO method is the time-dependent induced dipole moment $d(t)$, defined as

$$d(t) = -ev(z) = -ev \int \rho d\rho dz R^2 dR |\Psi(\rho, z, R, t)|^2 z. \quad (29)$$

The temporal variations of the induced dipole $d(t)$ obtained by the three different methods are shown in Fig. 4, in which we can see that the Ex-MCTDHF($K = 12$) curve is in close agreement with the 3D-grid curve even though the Ex-MCTDHF($K = 2$) and Ex-MCTDHF($K = 4$) curves exhibit oscillations in the longer time domain than 13 fs ($t > 13$ fs) in the absence of the laser pulse. The amplitude of the oscillations becomes smaller as K increases and the oscillation disappears when $K = 12$.

The amplitude of the induced dipole moment obtained by the two-state BO model is in good agreement with that obtained by the 3D-grid method in the early part of the laser pulse ($t \lesssim 5$ fs). This is because the two lowest electronic states ($1s\sigma_g$ and $2p\sigma_u$) are populated almost exclusively. During the later part of the pulse, higher-lying states become

populated, and consequently, the two-state BO method, in which higher-lying states are omitted, leads to a significant underestimation of the amplitude of $d(t)$.

C. Interpretation of the time-dependent wave function

In this section, in order to examine the temporal variations of time-dependent wave functions, we adopt two methods, that is, a method via the natural orbital decomposition in Sec. III C 1 and a method via the time-dependent potential-energy curves in Sec. III C 2. Both of these methods are general in the sense that they can be applied straightforwardly to larger many-electron molecules. In principle, these two methods can also be applied to interpret the response of any kind of wave function to an intense laser field.

1. Natural orbital decomposition

The results obtained by the time-dependent calculations above can be interpreted in terms of natural orbitals [33,40]. The electronic natural orbitals $\phi_j^{(\text{nat})}$ are defined as the orbitals that diagonalize the density matrix D_{jk}^e ,

$$\phi_j^{(\text{nat})}(z, \rho, t) = \sum_{k=1}^K \phi_k(z, \rho, t) u_{kj}, \quad (30)$$

where u_{jk} are the complex conjugated eigenvectors of D_{jk}^e ,

$$\sum_{k=1}^K D_{jk}^e u_{kl}^* = \eta_l u_{jl}^*. \quad (31)$$

Similarly, for the protonic natural orbitals $\chi_k^{(\text{nat})}$, we have

$$\chi_k^{(\text{nat})}(R, t) = \sum_{l=1}^K \chi_l(R, t) v_{lk}, \quad (32)$$

with

$$\sum_{k=1}^K D_{jk}^p v_{kl}^* = \eta_l v_{jl}^*. \quad (33)$$

The eigenvalues η_l shared by D_{jk}^e and D_{jk}^p are referred to as the natural populations [40,69] because they take real and positive values that satisfy

$$\sum_{l=1}^K \eta_l = 1. \quad (34)$$

Hereafter, we assume that the natural orbitals are sorted so that their populations fulfill the inequalities $\eta_1 \geq \eta_2 \geq \dots \geq \eta_K$.

If the natural orbitals are used in the expansion of the wave function, the coefficient matrix becomes diagonal [40,69] so that

$$C_{jk}^{(\text{nat})} = \delta_{jk} c_j^{(\text{nat})} = \sum_{l,m=1}^K u_{lj}^* C_{lm} v_{mk}^*. \quad (35)$$

The relation between the natural populations and $c_j^{(\text{nat})}$ reads

$$|c_j^{(\text{nat})}|^2 = \eta_j. \quad (36)$$

Therefore, the total wave function can be written using the natural orbitals as

$$\begin{aligned}\Psi(z, \rho, R, t) &= \sum_{j,k=1}^K C_{jk}(t) \phi_j(z, \rho, t) \chi_k(R, t) \\ &= \sum_{j=1}^K c_j^{(\text{nat})}(t) \phi_j^{(\text{nat})}(z, \rho, t) \chi_j^{(\text{nat})}(R, t),\end{aligned}\quad (37)$$

where the expansion coefficients $c_j^{(\text{nat})}(t)$ can be chosen to be real, positive numbers by a suitable adjustment of the phase of the orbitals.

It was recently suggested that the time-dependent natural orbitals for a model H_2^+ molecule in which its electron is restricted to move along the one-dimensional molecular axis can be obtained numerically as a solution of the equations of motion for the natural orbitals of a two-particle system [67]. Contrarily, in our approach, we do not calculate the natural orbitals directly as a solution of an equation of motion. We find it more straightforward to obtain the time-dependent wave function in the form described in the first row of Eq. (37), and then, the natural orbitals by the diagonalization of the one-particle density matrices as described in Eqs. (30)–(33).

In Fig. 5 we show the natural protonic orbitals $|\chi_j^{(\text{nat})}(R, t)|^2$ at three instants in time, $t = 0$ fs (before the laser-molecule interaction), $t = 14$ fs (after the laser pulse vanishes), and $t = 36$ fs (at the end of the simulation). Also shown in Fig. 5 is the total protonic density $P(R, t)$ defined in Eq. (27). The natural orbitals and the total density are related to each other as $R^2 \sum_{j=1}^K \eta_j |\chi_j^{(\text{nat})}(R, t)|^2 = P(R, t)$. In Fig. 6, we show the electronic natural orbital densities integrated over ρ , $\int \rho d\rho |\phi_j^{(\text{nat})}(z, \rho, t)|^2$, and the total electronic z density $P_e(z, t)$, defined as the total wave function integrated over R and ρ ,

$$P_e(z, t) = \int \rho d\rho R^2 dR |\Psi(\rho, z, R, t)|^2. \quad (38)$$

In both Figs. 5 and 6, the three natural orbitals having the largest natural populations η_j are shown.

We see in Figs. 5(a) and 6(a) that the total wave function is dominated initially by one pair of natural orbitals, $\phi_1^{(\text{nat})}(z, \rho, t)$ and $\chi_1^{(\text{nat})}(R, t)$, reflecting $\eta_1(t=0) = 0.99$. The third electronic natural orbital $\phi_3^{(\text{nat})}(z, \rho, t=0)$ has sharp peaks around the positions of the protons. The magnitude of these peaks decreases rapidly in the ρ direction, and therefore appear as the narrow peaks in the ρ -integrated density at around $z = \pm 0.5$ Å as shown in Fig. 6(a).

As a result of the laser-molecule interaction, the natural orbitals almost unpopulated initially become populated. As shown in Figs. 5(b) and 6(b), just after the laser pulse vanishes ($t = 14$ fs), we obtain $\eta_1 = 0.69$ and $\eta_2 = 0.11$, and, as shown in Figs. 5(c) and 6(c), after the further field-free propagation ($t = 36$ fs), we obtain $\eta_1 = 0.66$ and $\eta_2 = 0.10$.

In Fig. 5(c), we see that the two natural orbitals $\chi_1^{(\text{nat})}$ and $\chi_2^{(\text{nat})}$ having the highest populations are distributed in the completely separated regions of the internuclear distance R . The natural orbital $\chi_1^{(\text{nat})}$ describes the bound vibrational motion of H_2^+ , while $\chi_2^{(\text{nat})}$ describes the dissociating part

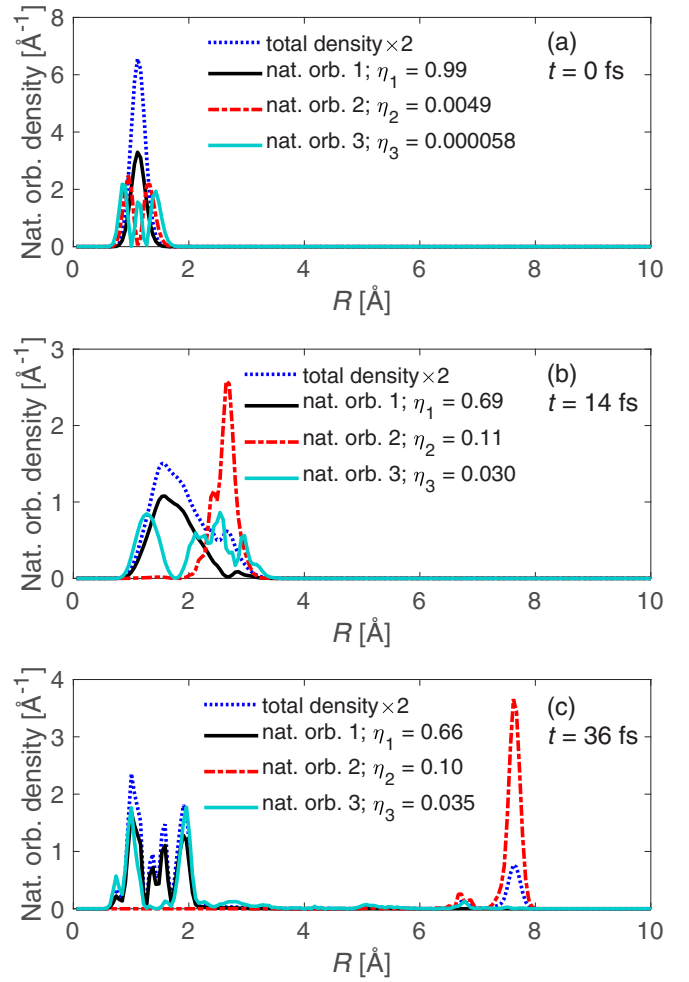


FIG. 5. Protonic natural orbital densities $R^2 |\chi_j^{(\text{nat})}(R, t)|^2$ for the three natural orbitals with the highest populations η_j at (a) $t = 0$ fs, (b) $t = 14$ fs, and (c) $t = 36$ fs. The natural orbitals are obtained from the Ex-MCTDHF wave function with $K = 12$. The laser parameters adopted here are the same as in Fig. 2; $I = 5 \times 10^{14}$ W/cm², $\lambda = 400$ nm, and $n_c = 10$. In all panels, the dotted line shows the total protonic density $P(R, t)$ multiplied by a factor of 2 for better visibility.

of the wave packet. The third most occupied natural orbital $\chi_3^{(\text{nat})}$ mainly describes the vibrational motion, but it also contributes to the dissociating part of the wave packet to a small extent. In the bound domain ($R < 3$ Å), we obtain the squared norm as $\int_0^{3\text{Å}} dR R^2 |\chi_3^{(\text{nat})}(R, t = 36\text{ fs})|^2 \approx 0.89$, and in the domain corresponding to dissociation ($R > 3$ Å), we obtain $\int_{3\text{Å}}^{\infty} dR R^2 |\chi_3^{(\text{nat})}(R, 36\text{ fs})|^2 \approx 0.11$. An inspection of the corresponding electronic natural orbitals shown in Fig. 6 confirms the picture obtained from the analysis of the protonic natural orbitals, that is, as shown in Fig. 6(c), the electronic natural orbital $\phi_1^{(\text{nat})}$ represents the localized wave packet at around $z = 0$ and the natural orbital $\phi_2^{(\text{nat})}$ represents the outgoing wave packet located at $z \approx \pm 4$ Å at $t = 36$ fs.

In a wave function calculated by the Ex-MCTDHF method, both the electronic orbitals and the protonic orbitals change dynamically in time. The attractive Coulomb interaction

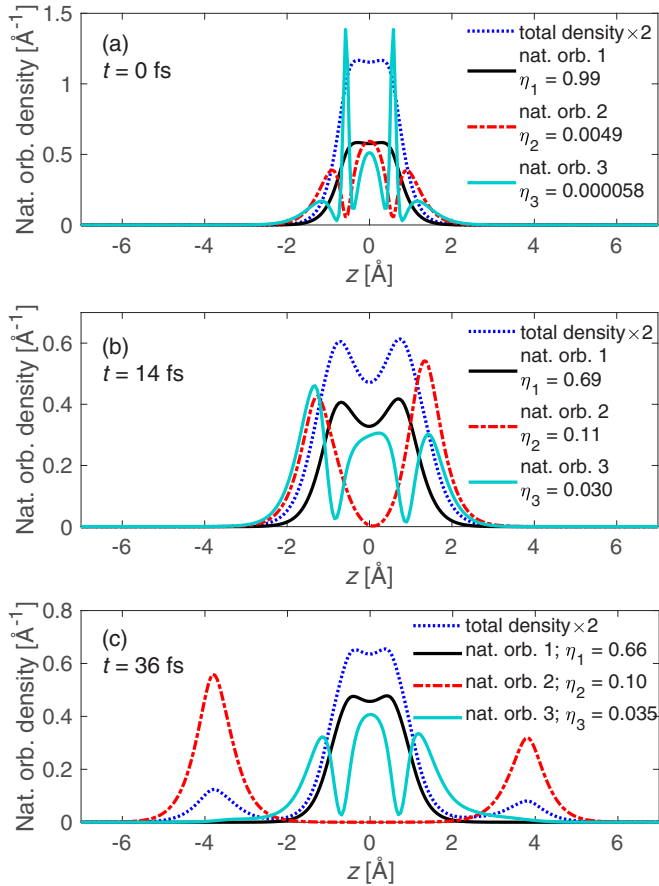


FIG. 6. Electronic natural orbital densities $\int \rho d\rho |\phi_j^{(\text{nat})}(z, \rho, t)|^2$ integrated over ρ for the three orbitals with the highest populations η_j at (a) $t = 0$ fs, (b) $t = 14$ fs, and (c) $t = 36$ fs obtained from the Ex-MCTDHF wave function with $K = 12$. The laser parameters adopted are the same as in Fig. 2; $I = 5 \times 10^{14}$ W/cm², $\lambda = 400$ nm, and $n_c = 10$. The dotted line shows the total electronic z density $P_e(z, t)$ multiplied by a factor of 2.

ensures that the term $c_2^{(\text{nat})}(t)\phi_2^{(\text{nat})}(z, \rho, t)\chi_2^{(\text{nat})}(R, t)$ in the total wave function represents a dissociating H_2^+ molecule in the form of a superposition of the dissociation products $\text{H}^+ + \text{H}$ and $\text{H} + \text{H}^+$. The electronic orbital $\phi_2^{(\text{nat})}(z, \rho, t)$ and the protonic orbital $\chi_2^{(\text{nat})}(R, t)$ adjust their shapes so that a dissociating wave packet is formed.

Even though the total wave function used in the calculation shown in Figs. 5 and 6 contains $K = 12$ configurations, we find that two of the most populated natural orbital pairs, $(\chi_j^{(\text{nat})}, \phi_j^{(\text{nat})})$, with $j = 1, 2$ are sufficient for describing the two main channels of the bound vibrational motion and the dissociation. This suggests that a minimal requirement for an Ex-MCTDHF wave function is $K =$ “the number of final channels,” and that one pair of natural orbitals, $(\chi_j^{(\text{nat})}, \phi_j^{(\text{nat})})$, describes the j th final channel. This is consistent with the results shown in Fig. 2(b), showing that the Ex-MCTDHF result with $K = 2$ reproduces the bifurcation of the vibrational wave function into one dissociating component and one vibrationally excited component, even though it exhibits a certain deviation from the direct 3D-grid result. It can be said that the natural orbitals with $K \geq 3$ having only small

populations need to be included for reproducing quantitatively the wave function. As shown in Figs. 5(c) and 6(c) for $t = 36$ fs, we have $\eta_j = 0.66, 0.10, 0.035, 0.018, 0.0056, 0.0024, 0.0013$, and 0.0010 for $1 \leq j \leq 8$ and $\eta_j < 10^{-3}$ for $9 \leq j \leq 12$, showing that η_1 and η_2 are much larger than η_j for $j > 2$.

2. Adiabatic potential-energy curves

In this section, we introduce the concept of time-dependent potential-energy curves and show how they can be constructed based on the Ex-MCTDHF wave function. Previously, several different approaches were proposed for constructing time-dependent potential-energy curves. Probably the best-known concept is the adiabatic and “field-following” potential-energy curve [8,70,71]. This time-dependent potential-energy curve is defined by the diagonalization of the electronic Hamiltonian having the laser-molecule interaction term. This means that at each point in time, Eq. (24) whose $h_e(z, \rho, 0)$ is replaced by $h_e(z, \rho, t)$ is solved, yielding a set of adiabatic potential-energy curves $\epsilon_j(R, t)$, which vary depending on both R and t .

Recently, the idea of the time-dependent BO approximation [72–74] and the idea of an exact factorization of an electron-nuclear wave function [75–83] were proposed and their applicabilities were demonstrated. In these cases, the electronic part of the factorized wave function can be used to define a single time-dependent potential-energy surface.

The time-dependent potential-energy curves introduced in this section are regarded as a reference with which we can understand the time-dependent behavior of the wave function. In order to construct the time-dependent potential-energy curves, we first need to have a total time-dependent wave function of the system. We start our discussion by deriving an alternative form of the Ex-MCTDHF equation of motion for the protonic orbitals. We first define an auxiliary protonic orbital as

$$\xi_j(R, t) = \sum_{k=1}^K C_{jk}(t)\chi_k(R, t), \quad (39)$$

so that the total wave function (10) reads

$$\Psi(z, \rho, R, t) = \sum_{j=1}^K \phi_j(z, \rho, t)\xi_j(R, t). \quad (40)$$

As discussed later in Eqs. (52)–(54), the same results are obtained for the effective potentials when $\xi_j(R, t)$ is defined in terms of the natural orbitals $\chi_j^{(\text{nat})}(R, t)$ as

$$\xi_j^{(\text{nat})}(R, t) = c_j^{(\text{nat})}(t)\chi_j^{(\text{nat})}(R, t), \quad (41)$$

so that the total wave function is written like

$$\Psi(z, \rho, R, t) = \sum_{j=1}^K \phi_j^{(\text{nat})}(z, \rho, t)\xi_j^{(\text{nat})}(R, t). \quad (42)$$

Unlike the protonic orbital $\chi_j(R, t)$ in the Ex-MCTDHF expansion (10), the ξ_j 's do not form an orthonormal set, that is, $\langle \xi_j(t) | \xi_k(t) \rangle = D_{jk}^e \neq \delta_{jk}$. By substituting the wave function (40) into the TDSE (9), we derive the equation of motion

for ξ_j as

$$\begin{aligned} i\hbar \frac{\partial \xi_j(R, t)}{\partial t} &= \sum_{k=1}^K \langle \phi_j | H(t) | \phi_k \rangle \xi_k(R, t) \\ &= h_p(R) \xi_j(R, t) + \sum_{k=1}^K H_{jk}(R, t) \xi_k(R, t), \end{aligned} \quad (43)$$

where $H_{jk}(R, t)$ is defined as

$$H_{jk}(R, t) = \langle \phi_j | h_e(t) | \phi_k \rangle + U_{jk}^p(R, t). \quad (44)$$

One can show that Eq. (43) is equivalent to the two equations, Eq. (12) for $\chi_j(R, t)$ and Eq. (13) for $C_{jk}(t)$.

As first suggested in Refs. [56,84], the form (40) can be employed for the construction of time-dependent adiabatic potential-energy curves, which can be used for the interpretation of the nuclear motion. We first write

$$\xi_k(R, t) = \sum_{j=1}^K A_{kj}(R, t) \zeta_j(R, t), \quad (45)$$

where $A_{kj}(R, t)$ is an R - and t -dependent unitary matrix. In Eq. (45), $\zeta_j(R, t)$ is a transformed protonic orbital that can be interpreted as the protonic wave function propagating on the j th adiabatic potential-energy curve $V_j(R, t)$ derived below in Eq. (51). After substituting (45) into Eq. (43), we obtain the equation for $\zeta_j(R, t)$,

$$\begin{aligned} i\hbar \frac{\partial \zeta_j(R, t)}{\partial t} &= h_p(R) \zeta_j(R, t) + \sum_{k=1}^K \tilde{H}_{jk}(R, t) \zeta_k(R, t) \\ &+ \sum_{k=1}^K [Y_{jk}(R, t) - iB_{jk}(R, t)] \zeta_k(R, t), \end{aligned} \quad (46)$$

where

$$\begin{aligned} \tilde{H}_{jk}(R, t) &= \sum_{l,m=1}^K A_{lj}^*(R, t) H_{lm}(R, t) A_{mk}(R, t), \quad (47) \\ Y_{jk}(R, t) &= \frac{-\hbar^2}{2\mu_p} \sum_{l=1}^K \left[A_{lj}^*(R, t) \frac{1}{R^2} \frac{\partial}{\partial R} \left(R^2 \frac{\partial A_{lk}(R, t)}{\partial R} \right) \right. \\ &\quad \left. + 2A_{lj}^*(R, t) \frac{\partial A_{lk}(R, t)}{\partial R} \frac{\partial}{\partial R} \right], \quad (48) \end{aligned}$$

and

$$B_{jk}(R, t) = \hbar \sum_{l=1}^K A_{lj}^*(R, t) \frac{\partial A_{lk}(R, t)}{\partial t}. \quad (49)$$

If we neglect $Y_{jk}(R, t)$ and $B_{jk}(R, t)$, which corresponds to an adiabatic approximation with respect to R and t as explained below, and if we choose $A_{jk}(R, t)$ so that $\tilde{H}_{jk}(R, t)$ becomes a diagonal matrix at each value of R and t , the coupled Schrödinger equation (46) is decoupled into K equations

for the respective protonic orbitals $\zeta_j(R, t)$,

$$i\hbar \frac{\partial \zeta_j(R, t)}{\partial t} = \left[-\frac{\hbar^2}{2\mu_p} \frac{1}{R^2} \frac{\partial}{\partial R} \left(R^2 \frac{\partial}{\partial R} \right) + V_j(R, t) \right] \zeta_j(R, t). \quad (50)$$

The diagonal terms

$$V_j(R, t) = \tilde{H}_{jj}(R, t) + \frac{e^2}{R} \quad (51)$$

are interpreted as time-dependent potential-energy curves on which the protonic orbitals $\zeta_j(R, t)$ are being propagated [56,84]. Because the potential-energy curves $V_j(R, t)$ are defined in terms of the electronic orbitals, $V_j(R, t)$ can be used for the interpretation of the time-dependent behavior of the wave function only when the electron and the protons are located approximately in the same spatial region. If the electronic orbitals are spatially located at around $z \sim z_0$, we do not expect that $V_j(R, t)$ provides useful information at the internuclear distances $R \gg z_0$ even if $V_j(R, t)$ is mathematically well defined for all R .

The definition (51) of the adiabatic potential-energy curves $V_j(R, t)$ is invariant under unitary transformations of the electronic orbitals, as shown below. Therefore, we can use any orbital set obtained by a unitary transformation of the original orbital set, such as the natural orbitals $\phi_j^{(\text{nat})}(z, \rho, t)$ defined in (30), to evaluate the adiabatic potential-energy curves. If we assume that a set of orbitals $\phi'_j(z, \rho, t)$ is transformed from the original set of orbitals $\phi_j(z, \rho, t)$ by a unitary transformation u_{jk} as

$$\phi'_j(z, \rho, t) = \sum_{k=1}^K u_{kj} \phi_k(z, \rho, t), \quad (52)$$

the $H_{jk}(R, t)$ matrix expressed in terms of the transformed orbitals becomes

$$H'_{jk}(R, t) = \sum_{lm} u_{lj}^* H_{lm}(R, t) u_{mk}. \quad (53)$$

If $H_{jk}(R, t)$ is diagonalized by $A_{jk}(R, t)$, $H'_{jk}(R, t)$ is diagonalized by $A'_{jk}(R, t) = \sum_l u_{lj}^* A_{lk}(R, t)$, because

$$\begin{aligned} \sum_{lm} A'_{lj}^* H'_{lm}(R, t) A'_{mk} &= \sum_{lm} A_{lj}^* H_{lm}(R, t) A_{mk} \\ &= \tilde{H}_{jj}(R, t), \end{aligned} \quad (54)$$

and consequently $H'_{jk}(R, t)$ has the same eigenvalues as $H_{jk}(R, t)$.

The approximation of dropping both $Y_{jk}(R, t)$ and $B_{jk}(R, t)$ can be regarded as an adiabatic approximation with respect to the two variables, the internuclear distance R and the time t . This approximation becomes appropriate only when $A_{jk}(R, t)$ varies slowly as a function of both R and t . In the limit of the slow change of $A_{jk}(R, t)$ with variations of R and t , the adiabatic approximation becomes exact, and no transitions would occur between the different potential-energy curves. This means in particular that the norm $\int dR R^2 |\zeta_j(R, t)|^2$ of each nuclear wave packet is constant in time.

The nonadiabatic transitions are governed by the matrix operators $Y_{jk}(R, t)$ and $B_{jk}(R, t)$. We also note that the

adiabatic potential-energy curves $V_j(R, t)$ can be calculated independently of the nonadiabatic coupling matrices $Y_{jk}(R, t)$ and $B_{jk}(R, t)$. Furthermore, as shown in Eqs. (47)–(49), differentiation of the unitary transformation matrix $A_{jk}(R, t)$ with respect to R is only needed for the evaluation of $Y_{jk}(R, t)$ and $B_{jk}(R, t)$, not for the evaluation of $V_j(R, t)$.

By inserting Eq. (45) into Eq. (40), we obtain

$$\begin{aligned} \Psi(z, \rho, R, t) &= \sum_{j,k=1}^K \phi_j(z, \rho, t) A_{jk}(R, t) \zeta_k(R, t) \\ &= \sum_{k=1}^K \varphi_k(z, \rho, R, t) \zeta_k(R, t). \end{aligned} \quad (55)$$

In the second line of Eq. (55), we define the time- and R -dependent adiabatic electronic states

$$\varphi_k(z, \rho, R, t) = \sum_{j=1}^K \phi_j(z, \rho, t) A_{jk}(R, t). \quad (56)$$

In terms of the adiabatic electronic states $\varphi_k(z, \rho, R, t)$, we can write the adiabatic potential curve $V_j(R, t)$ as

$$\begin{aligned} V_j(R, t) &= \int \rho d\rho dz \varphi_j^*(z, \rho, R, t) [h_e(t) + U(z, \rho, R)] \\ &\quad \times \varphi_j(z, \rho, R, t) + \frac{e^2}{R}. \end{aligned} \quad (57)$$

The expression (55) for the total wave function looks very similar to that in Eq. (23) for the BO approximation, but the adiabatic electronic states $\varphi_k(\rho, z, R, t)$ depend on t in Eq. (55) while the corresponding adiabatic electronic states $\phi_j^{\text{BO}}(z, \rho; R)$ in Eq. (23) do not depend on t .

In Fig. 7, we show the instantaneous adiabatic potential-energy curves $V_j(R, t)$ defined in Eq. (51) at the three different instants in time, $t = 0$, $t = 14$ fs, and $t = 36$ fs, which are the same as those adopted in Figs. 5 and 6. At $t = 0$, as shown in Fig. 7(a), we also draw the two lowest energy BO potential-energy curves $V_j^{\text{BO}}(R)$ ($j = 1\sigma_g, 2p\sigma_u$), defined as

$$V_j^{\text{BO}}(R) = \frac{e^2}{R} + \epsilon_j(R), \quad (58)$$

where $\epsilon_j(R)$ is a solution of Eq. (24). We see in Fig. 7(a) that the adiabatic potential-energy curve with the lowest energy perfectly overlaps with the $1\sigma_g$ BO potential-energy curve in the region $R < 2$ Å. The second lowest adiabatic potential-energy curve $V_2(R, t = 0)$, shown with a red solid line in Fig. 7(a), is much higher in energy than the $V_{2p\sigma_u}^{\text{BO}}(R)$ curve. In general, the higher-lying adiabatic potential-energy curves at $t = 0$ are expected to exhibit a certain deviation from the excited-state BO potential-energy curves, because the orbitals from which the adiabatic potential-energy curves are extracted are optimized for the electronic ground state.

After the interaction with the laser pulse at $t = 14$ fs, we can see in Fig. 7(b) that the two lowest-energy adiabatic potential-energy curves, $V_1(R, 14$ fs) and $V_2(R, 14$ fs), become close in energy in the region around $R = 3$ Å and that the lower curve $V_1(R, 14$ fs) develops a broad well having a minimum at $R \approx 1$ Å and a flat region at $R \approx 3.5$ Å. At

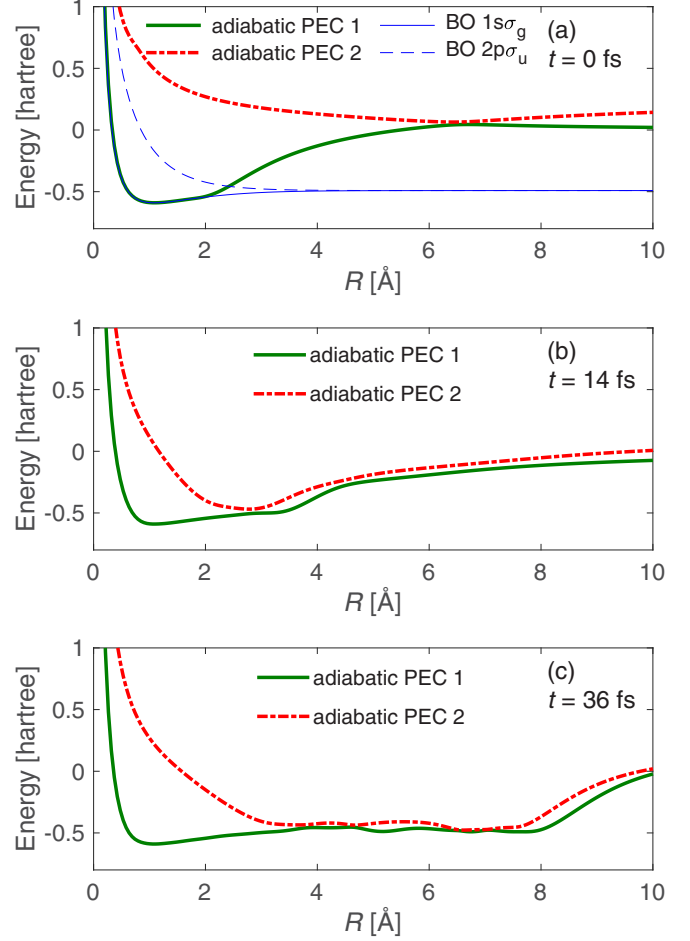


FIG. 7. Adiabatic potential-energy curves (PECs) $V_j(R, t)$ obtained from the Ex-MCTDHF wave function with $K = 12$. The laser parameters are $I = 5 \times 10^{14}$ W/cm², $\lambda = 400$ nm, and $n_c = 10$, which are the same as those adopted in Figs. 2, 5, and 6. In (a), the $1\sigma_g$ and $2p\sigma_u$ BO potential-energy curves are shown using thin lines. The BO $1\sigma_g$ curve and the adiabatic PEC 1 perfectly overlap in the region $R < 2$ Å.

$t = 36$ fs, as shown in Fig. 7(c), the potential wells stretches further towards the longer internuclear distance region until at $R \approx 9$ Å.

In Fig. 8, we show the normalized adiabatic protonic orbital densities $P_j^{(\text{adb})}(R, t)$, defined as

$$P_j^{(\text{adb})}(R, t) = \frac{R^2 |\zeta_j(R, t)|^2}{N_j(t)}, \quad (59)$$

where

$$N_j(t) = \int dR R^2 |\zeta_j(R, t)|^2 \quad (60)$$

is the squared norm of the protonic orbital ζ_j . We show in Fig. 8 the normalized protonic orbitals at the same time instants as the corresponding potential-energy curves shown in Fig. 7. In Fig. 8, the numerical values N_1 and N_2 for the two adiabatic orbitals are also shown. In Fig. 8(a), in which the adiabatic orbital densities are shown at $t = 0$, we see that the $\zeta_1(R, t = 0)$ is centered at the equilibrium

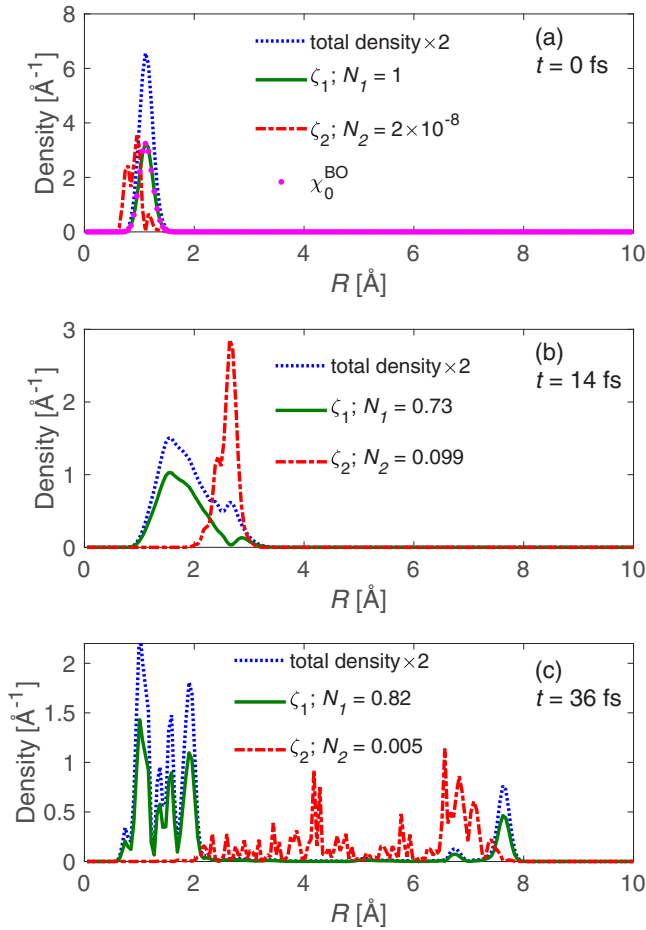


FIG. 8. Normalized density $P_j^{(\text{adb})}(R, t)$ ($j = 1, 2$) defined in Eq. (59) of the adiabatic protonic orbitals. The two adiabatic protonic orbitals having the largest squared norms N_j are shown. The dotted line indicates the total protonic density $P(R, t)$ defined in Eq. (27), multiplied by a factor 2. In (a), the wave function of the vibrational ground state $\chi_0^{\text{BO}}(R)$ defined in Eq. (26) is also shown, which is obtained by the BO method. The adiabatic protonic orbitals are obtained from an Ex-MCTDHF wave function with $K = 12$. The laser parameters are the same as those in Fig. 7; $I = 5 \times 10^{14}$ W/cm², $\lambda = 400$ nm, and the number of optical cycles $n_c = 10$.

internuclear distance $R_e \approx 1.1$ Å, and that $R^2|\zeta_j(R, 0)|^2$ overlaps completely with the BO ground state density $R^2|\chi_0^{\text{BO}}(R)|^2$, where $\chi_0^{\text{BO}}(R)$ stands for the BO vibrational ground-state wave function defined in Eq. (26). The density of the adiabatic protonic orbital $\zeta_2(R, 0)$ for the first excited-state potential-energy curve has a very small squared norm of 2×10^{-8} .

As a result of the laser-molecule interaction, nonadiabatic transitions to the excited potential-energy curves are induced. As shown in Fig. 8(b), at $t = 14$ fs, the bifurcation of the protonic wave packet proceeds and the squared norm of the excited protonic orbital $\zeta_2(R, t = 14$ fs) increases to 0.099. The squared norm of $\zeta_2(R, t)$ then decreases to 0.005 at $t = 36$ fs, as can be seen in Fig. 8(c). At $t = 36$ fs, the largest contribution to the total wave function comes from the orbital $\zeta_1(R, 36$ fs), which contains one component localized in the region $0.5 \text{ \AA} < R < 2.5 \text{ \AA}$ representing the bound vibrational

motion and the other component centered at $R \approx 7.7$ Å. These two components are consistent with the two potential wells located at $R \approx 1$ Å and at $R \approx 8$ Å in the adiabatic potential-energy curve at $t = 36$ fs shown in Fig. 7(c).

Based on the adiabatic time-dependent potential curves shown in Fig. 7 and the adiabatic protonic orbitals shown in Fig. 8, we can interpret the motion of the nuclear wave packet as follows:

(i) Before the laser-molecule interaction, the nuclear wave function can be represented by a single protonic orbital localized in the bound well of the lowest adiabatic potential-energy curve.

(ii) The laser pulse induces nonadiabatic coupling between the lowest potential-energy curve and the excited potential-energy curve, so that, after the laser-molecule interaction, the protonic wave function is split into one protonic orbital on the lowest adiabatic potential-energy curve and the other protonic orbital on the second lowest adiabatic potential-energy curve.

(iii) The orbital evolving on the lowest adiabatic curve, shown with a solid green line in Figs. 8(b) and 8(c), splits into two components; one corresponding to the bound vibrational motion and the other corresponding to the dissociation.

(iv) These two components follow the position of the two potential wells appearing in the lowest adiabatic potential-energy curve in Figs. 7(b) and 7(c). This idea of dissociation as a bound vibrational wave packet evolving on a time-dependent potential is different from the idea of a time-dependent wave packet moving on a time-independent potential-energy curve.

(v) The orbital evolving on the excited adiabatic curve, shown with a red solid line in Figs. 8(b) and 8(c), is gradually transferred to the lowest adiabatic curve by the nonadiabatic coupling described by $Y_{jk}(R, t)$ in Eq. (48) and $B_{jk}(R, t)$ in Eq. (49).

(vi) Finally, almost all the population on the excited adiabatic curve vanishes, and at $t = 36$ fs, we have a population of only $N_2(36 \text{ fs}) \approx 0.005$ as can be seen in Fig. 8(c). The adiabatic electronic state $\varphi_1(z, \rho, R, t = 36 \text{ fs})$ corresponding to the lowest adiabatic potential-energy curve $V_1(R, t = 36 \text{ fs})$ can describe both the vibration in the bound well and the dissociation into $\text{H} + \text{H}^+$, because the electronic density varies depending on R : around $R \approx 1$ Å, $\varphi_1(z, \rho, R, 36 \text{ fs})$ is nonzero for $|z| < 1$ Å, and around $R \approx 8$ Å, $\varphi_1(z, \rho, R, 36 \text{ fs})$ is distributed at around $z \approx \pm 4$ Å.

There are two forms of the nonadiabatic coupling, one related to the nonadiabaticity in t described by the matrix $B_{jk}(R, t)$ in Eq. (49) and the other related to the nonadiabaticity in R described by the matrix $Y_{jk}(R, t)$ in Eq. (48). In order to examine which one of $B_{jk}(R, t)$ and $Y_{jk}(R, t)$ gives a larger contribution to the nonadiabatic transition of $\zeta_2(R, t)$ from $V_2(R, t)$ to $V_1(R, t)$, we evaluate numerically $B_{jk}(R, t)$ and $Y_{jk}(R, t)$ for $j = 1$ and $k = 2$. The matrix $B_{jk}(R, t)$ can be conveniently evaluated by differentiating Eq. (47) with respect to time as [71]

$$B_{jk}(R, t) = \frac{\sum_{l,m=1}^K A_{lj}^*(R, t) \frac{\partial H_{lm}(R, t)}{\partial t} A_{mk}(R, t) - \delta_{jk} \frac{\partial V_k(R, t)}{\partial t}}{V_k(R, t) - V_j(R, t)}, \quad (61)$$

where $\partial H_{lm}(R, t)/\partial t$ can be obtained numerically using the definition Eq. (44) and the equation of motion (11). The numerical values of $A_{ij}^*(\partial/\partial R)A_{lk}$ and $A_{ij}^*(\partial^2/\partial R^2)A_{lk}$ appearing in the definition (48) of $Y_{jk}(R, t)$ are obtained using the same finite-difference scheme as adopted for the protonic kinetic-energy operator (see Appendix for details).

We find that at $t = 14$ fs, as shown in Figs. 7(b) and 8(b), $|B_{12}(R, t)\zeta_2(R, t)| \gg |Y_{12}(R, t)\zeta_2(R, t)|$ for $0 < R < 10$ Å. This is because of the small factor of $1/\mu_p \approx 0.001$ in $Y_{12}(R, t)$. We find $B_{12}(R = 2.5$ Å, 14 fs) $\approx 0.1E_h$ at the internuclear distance $R = 2.5$ Å around which $\zeta_2(R, 14$ fs) is located as shown in Fig. 8(b).

IV. CONCLUSIONS AND SUMMARY

We have shown that the Ex-MCTDHF methods works well to describe dissociation and excitation of H_2^+ induced by the irradiation of an intense laser pulse. As long as the number of expansion terms K included in the Ex-MCTDHF expansion is equal to or larger than 2, the wave-packet bifurcation into a dissociating component and a vibrationally excited component is reproduced, and for $K > 8$, a good quantitative agreement between the results obtained by the Ex-MCTDHF method and those obtained by the direct 3D-grid method is achieved.

We have also introduced two methods that can be used for the interpretation of a time-dependent electroprotonic wave function. First, we expanded the total wave function in terms of the natural orbitals and found that different natural orbitals correspond to different channels, that is, one natural orbital pair represents the vibrational excitation while the other pair represents the dissociation. This shows that, using the Ex-MCTDHF method, we can describe a dissociating wave function representing the spatially correlated motion of electrons and nuclei bound through the attractive Coulomb interaction. In the second method, we calculated time-dependent adiabatic potential-energy curves by diagonalizing the Hamiltonian governing the motion of the protonic orbitals. We showed that the lowest adiabatic potential-energy curve is composed of one time-independent well located at around $R = 1$ Å and one

broad time-dependent well whose outer barrier moves towards the longer internuclear distance as time goes on. The part of the protonic wave packet trapped in the time-independent well corresponds to the bound vibrational motion, and the part located in the time-dependent part of the adiabatic potential-energy curve corresponds to the dissociation. Our results show that dissociation in general can be interpreted as a bound vibrational wave packet evolving on a time-dependent potential-energy curve.

The present study on laser-driven H_2^+ can be regarded as the first step toward the application of the Ex-MCTDHF method to many-electron polyatomic molecules interacting with a light field, in which both the electronic and protonic parts of the wave function need to be antisymmetrized. The next step would be to investigate time-dependent dynamics of laser-driven H_2 , whose ground-state wave function has already been obtained by the Ex-MCTDHF method [48].

ACKNOWLEDGMENT

This research was supported by JSPS KAKENHI Grants No. JP15K17805, No. JP18K05024, and No. JP15H05696.

APPENDIX: NUMERICS

1. Ex-MCTDHF

The orbitals are discretized on an equidistant grid with mesh width $\Delta z = \Delta \rho = \Delta R = 0.053$ Å ($=0.1a_0$). The spatial extent of the computational box is $|z| < z_{\max} = 13.3$ Å, $R < R_{\max} = 13.3$ Å, and $\rho < \rho_{\max} = 5.3$ Å. We write the electronic orbitals as

$$\phi_j(z, \rho) = \frac{f(z, \rho)}{\sqrt{\rho}}, \quad (\text{A1})$$

and define

$$f_{p,q} = f(z_p, \rho_q), \quad (\text{A2})$$

where (z_p, ρ_q) is a point on the computational grid; $p = 1, \dots, p_{\max}$ and $q = 1, \dots, q_{\max}$ with $\rho_1 = \Delta \rho$. The part of the kinetic-energy operator depending on ρ is approximated as described in Ref. [85],

$$\frac{1}{\sqrt{\rho}} \frac{\partial}{\partial \rho} \left(\rho \frac{\partial}{\partial \rho} \frac{f(z_p, \rho_q)}{\sqrt{\rho}} \right) \approx \begin{cases} \frac{1}{(\Delta \rho)^2} \left(-\frac{\rho_{3/2}}{\rho_1} f_{p,1} + \frac{\rho_{3/2}}{\sqrt{\rho_1 \rho_2}} f_{p,2} \right) & \text{if } q = 1, \\ \frac{1}{(\Delta \rho)^2} \left(\frac{\rho_{q-1/2}}{\sqrt{\rho_{q-1} \rho_q}} f_{p,q-1} - \frac{\rho_{q+1/2} + \rho_{q-1/2}}{\rho_q} f_{p,p} + \frac{\rho_{q+1/2}}{\sqrt{\rho_{q+1} \rho_q}} f_{p,q+1} \right) & \text{if } 1 < q < q_{\max}, \end{cases} \quad (\text{A3})$$

where $\rho_{q+1/2} = (\rho_q + \rho_{q+1})/2$. Equation (A3) correctly incorporates the boundary condition $\partial \phi_j(z, 0)/\partial \rho = 0$. For the second derivatives with respect to z , we employ a symmetric three-point formula,

$$\frac{\partial^2 f(z_p, \rho_q)}{\partial z^2} \approx \frac{f_{p-1,q} - 2f_{p,q} + f_{p+1,q}}{(\Delta z)^2}. \quad (\text{A4})$$

The protonic orbitals are discretized on a grid with grid points $R_k = k \Delta R$, $k = 1, \dots, k_{\max}$. We employ a formula similar to Eq. (A4) to approximate $\partial^2/\partial R^2$ appearing in the protonic kinetic-energy operator.

An absorbing imaginary potential is employed to prevent unphysical reflections from the boundary of the computational

domain. Using the function

$$w(a, x) = \begin{cases} -i(|x| - a)^3 & \text{for } |x| > a, \\ 0 & \text{otherwise,} \end{cases} \quad (\text{A5})$$

the total absorbing potential added to the Hamiltonian is defined as

$$\begin{aligned} W(z, \rho, R) &= W^e(z, \rho) + W^p(R) \\ &= w(\gamma z_{\max}, z) + w(\gamma \rho_{\max}, \rho) + w(\gamma R_{\max}, R), \end{aligned} \quad (\text{A6})$$

where $\gamma = 0.8$.

The mean-field potentials defined in Eqs. (16) and (17) are calculated in a way similar to that presented in Ref. [86]. We

first define the discrete version of the Coulomb potential,

$$U_{pq,k} = U(z_p, \rho_q, R_k), \quad (\text{A7})$$

where $U(z, \rho, R)$ is defined in Eq. (7). As a second step, we compute an approximate singular value decomposition of $U_{pq,k}$,

$$U_{pq,k} \approx \sum_{\ell=1}^{\ell_{\max}} s_{\ell} u_{pq,\ell} v_{k\ell}, \quad (\text{A8})$$

where s_{ℓ} are the singular values. For all calculations shown in the present study, we include $\ell_{\max} = 75$ of the largest singular values in the sum over ℓ in Eq. (A8).

After calculating the singular value decomposition of $U_{pq,k}$, we approximate the mean-field potentials (16) and (17) as

$$\begin{aligned} U^e(z_p, \rho_q) &= \langle \chi(R) | U(z_p, \rho_q, R) | \chi'(R) \rangle \\ &\approx \Delta R \sum_{\ell=1}^{\ell_{\max}} u_{pq,\ell} s_{\ell} \sum_k v_{k\ell} \chi^*(R_k) \chi'(R_k) R_k^2, \end{aligned} \quad (\text{A9})$$

$$\begin{aligned} U^p(R_k) &= \langle \phi(z, \rho) | U(z, \rho, R_k) | \phi'(z, \rho) \rangle \\ &\approx \Delta \rho \Delta z \sum_{\ell=1}^{\ell_{\max}} v_{k\ell} s_{\ell} \sum_{pq} u_{pq,\ell} \phi^*(z_p, \rho_q) \phi'(z_p, \rho_q) \rho_q. \end{aligned} \quad (\text{A10})$$

Without making the approximation (A8), the computational time required for obtaining $U^p(R_k, t)$ at all grid points R_k ($k = 1, \dots, k_{\max}$) would be proportional to $N = p_{\max} q_{\max} k_{\max}$. However, when we use Eq. (A10), the computational time is proportional to $N' = p_{\max} q_{\max} \ell_{\max}$, which makes this approach favorable if $\ell_{\max} < k_{\max}$. In the calculations presented in the present paper, this condition is satisfied, because $k_{\max} \approx 250$ and $\ell_{\max} = 75$.

The time stepping of the electronic orbitals is done in the following way. We first write the equation of motion (11) for the electronic orbitals as

$$i\hbar \frac{\partial \boldsymbol{\phi}(t)}{\partial t} = [T_{\text{kin}} + eE(t)vz + W^e(z, \rho)] \boldsymbol{\phi}(t) + \mathbf{B}(t) \boldsymbol{\phi}(t), \quad (\text{A11})$$

where $\boldsymbol{\phi} = (\phi_1, \phi_2, \dots, \phi_K)^T$ is an array of orbitals, T_{kin} is the kinetic-energy operator, and $\mathbf{B}(t)$ contains all other nonlinear terms in Eq. (11). We assume that $\mathbf{B}(t)$ is constant during a short time step Δt , and evolve the orbitals in time according to

$$\begin{aligned} \boldsymbol{\phi}(t + \Delta t) &\approx e^{-i\tau[eE(t)vz + W^e(z, \rho)]} e^{-i\tau T_{\text{kin}}} e^{-i2\tau \mathbf{B}(t)} e^{-i\tau T_{\text{kin}}} \\ &\times e^{-i\tau[eE(t)vz + W^e(z, \rho)]} \boldsymbol{\phi}(t), \end{aligned} \quad (\text{A12})$$

where $\tau = \Delta t/2\hbar$. The exponentiation of the $eE(t)vz$ and $W^e(z, \rho)$ is trivial, since these operators have a diagonal grid representation. The term $e^{-i\tau T_{\text{kin}}} \boldsymbol{\phi}$ is evaluated with the Crank-Nicolson method [87], and $e^{-i2\tau \mathbf{B}(t)} \boldsymbol{\phi}$ with the Lanczos method [88]. We use $\Delta t = 0.0025\hbar/E_h \approx 0.06$ as. The integration of the equation of motion (12) for the protonic orbitals is performed in a similar way as the integration for the electronic orbitals described above. The equation of motion (13) for the coefficients $C_{jk}(t)$ is integrated by using the Lanczos method in which $\langle \phi_j | \chi_k | H(t) | \phi_l | \chi_m \rangle$ is assumed to be constant during a short time step Δt .

2. Two-state BO model

In order to obtain the $1s\sigma_g$ and $2p\sigma_u$ potential-energy curves, we solve the eigenvalue equation (24) at the different values of R at $R_k = k\Delta R$, $k = 1, \dots, k_{\max}$, corresponding to the same R grid as that adopted in the calculation of the protonic Ex-MCTDHF orbitals. We solve Eq. (24) using the same discretization of the electronic wave functions as described above in Appendix 1. After obtaining $\epsilon_j(R_k)$, $j = 1s\sigma_g, 2p\sigma_u$ and $\langle \phi_{1s\sigma_g}^{\text{BO}} | z | \phi_{2p\sigma_u}^{\text{BO}} \rangle$, we solve Eq. (25) assuming the same R discretization as that adopted for the protonic Ex-MCTDHF orbitals, using the Crank-Nicolson method to exponentiate the kinetic-energy operator, and the Lanczos method for the other operators. We adopted an absorbing potential $W^p(R)$ defined in Eq. (A6) to prevent reflections of outgoing parts of the protonic wave packet.

3. 3D-grid method

The total wave function is represented as a 3D array,

$$\Psi_{pqk}(t) = \Psi(z_p, \rho_q, R_k, t), \quad (\text{A13})$$

where z_p , ρ_q , and R_k are the same grid points as those used in the Ex-MCTDHF method and the two-state BO model. The kinetic-energy operators are approximated using the same finite-difference scheme as that used for the Ex-MCTDHF method, for example, as

$$\begin{aligned} \frac{\partial^2 \Psi(z_p, \rho_q, R_k, t)}{\partial z^2} \\ \approx \frac{\Psi_{(p-1)qk}(t) - 2\Psi_{pqk}(t) + \Psi_{(p+1)qk}(t)}{(\Delta z)^2}. \end{aligned} \quad (\text{A14})$$

For the time stepping, we use a split-operator scheme similar to Eq. (A12), and employ the Crank-Nicolson method to evaluate the exponentiation of the kinetic-energy operators. We adopted the same absorbing potential given by Eq. (A6) to prevent reflections from the grid boundary.

[1] T. Okino, Y. Furukawa, P. Liu, T. Ichikawa, R. Itakura, K. Hoshina, K. Yamanouchi, and H. Nakano, Coincidence momentum imaging of ultrafast hydrogen migration in methanol and its isotopomers in intense laser fields, *Chem. Phys. Lett.* **423**, 220 (2006).

[2] T. Ando, A. Shimamoto, S. Miura, K. Nakai, H. Xu, A. Iwasaki, and K. Yamanouchi, Wave packet bifurcation in ultrafast hydrogen migration in CH_3OH^+ by pump-probe coincidence momentum imaging with few-cycle laser pulses, *Chem. Phys. Lett.* **624**, 78 (2015).

- [3] Y. H. Jiang, A. Rudenko, O. Herrwerth, L. Foucar, M. Kurka, K. U. Kühnel, M. Lezius, M. F. Kling, J. van Tilborg, A. Belkacem, K. Ueda, S. Düsterer, R. Treusch, C. D. Schröter, R. Moshhammer, and J. Ullrich, Ultrafast Extreme Ultraviolet Induced Isomerization of Acetylene Cations, *Phys. Rev. Lett.* **105**, 263002 (2010).
- [4] M. El-Amine Madjet, O. Vendrell, and R. Santra, Ultrafast Dynamics of Photoionized Acetylene, *Phys. Rev. Lett.* **107**, 263002 (2011).
- [5] M. Kübel, R. Siemering, C. Burger, N. G. Kling, H. Li, A. S. Alnaser, B. Bergues, S. Zhrebttsov, A. M. Azzeer, I. Ben-Itzhak, R. Moshhammer, R. de Vivie-Riedle, and M. F. Kling, Steering Proton Migration in Hydrocarbons using Intense Few-Cycle Laser Fields, *Phys. Rev. Lett.* **116**, 193001 (2016).
- [6] K. Takatsuka and T. Yonehara, Exploring dynamical electron theory beyond the Born-Oppenheimer framework: From chemical reactivity to non-adiabatically coupled electronic and nuclear wavepackets on-the-fly under laser field, *Phys. Chem. Chem. Phys.* **13**, 4987 (2011).
- [7] S. Chelkowski, T. Zuo, O. Atabek, and A. D. Bandrauk, Dissociation, ionization, and Coulomb explosion of H_2^+ in an intense laser field by numerical integration of the time-dependent Schrödinger equation, *Phys. Rev. A* **52**, 2977 (1995).
- [8] I. Kawata, H. Kono, and Y. Fujimura, Adiabatic and diabatic responses of H_2^+ to an intense femtosecond laser pulse: Dynamics of the electronic and nuclear wave packet, *J. Chem. Phys.* **110**, 11152 (1999).
- [9] A. D. Bandrauk, S. Chelkowski, and H. S. Nguyen, Attosecond localization of electrons in molecules, *Int. J. Quantum Chem.* **100**, 834 (2004).
- [10] I. Maruyama, T. Sako, and K. Yamanouchi, Time-dependent nuclear wavepacket dynamics of H_2^+ by quasi-stationary Floquet approach, *J. Phys. B* **37**, 3919 (2004).
- [11] G. Paramonov, Ionization and dissociation of simple molecular ions in intense infrared laser fields: Quantum dynamical simulations for three-dimensional models of HD^+ and H_2^+ , *Chem. Phys. Lett.* **411**, 350 (2005).
- [12] X. M. Tong and C. D. Lin, Dynamics of Light-Field Control of Molecular Dissociation at the Few-Cycle Limit, *Phys. Rev. Lett.* **98**, 123002 (2007).
- [13] M. F. Kling, C. Siedschlag, A. J. Verhoef, J. I. Khan, M. Schultze, T. Uphues, Y. Ni, M. Uiberacker, M. Drescher, F. Krausz, and M. J. J. Vrakking, Control of electron localization in molecular dissociation, *Science* **312**, 246 (2006).
- [14] B. Abeln, J. V. Hernández, F. Anis, and B. D. Esry, Comparison of theoretical analyses of intense-laser-induced molecular dissociation, *J. Phys. B* **43**, 155005 (2010).
- [15] P. Lan, E. J. Takahashi, and K. Midorikawa, Efficient control of electron localization by subcycle waveform synthesis, *Phys. Rev. A* **86**, 013418 (2012).
- [16] N. G. Kling, K. J. Betsch, M. Zohrabi, S. Zeng, F. Anis, U. Ablikim, B. Jochim, Z. Wang, M. Kübel, M. F. Kling, K. D. Carnes, B. D. Esry, and I. Ben-Itzhak, Carrier-Envelope Phase Control over Pathway Interference in Strong-Field Dissociation of H_2^+ , *Phys. Rev. Lett.* **111**, 163004 (2013).
- [17] T. Rathje, A. M. Sayler, S. Zeng, P. Wustelt, H. Figger, B. D. Esry, and G. G. Paulus, Coherent Control at Its Most Fundamental: Carrier-Envelope-Phase-Dependent Electron Localization in Photodissociation of a H_2^+ Molecular Ion Beam Target, *Phys. Rev. Lett.* **111**, 093002 (2013).
- [18] J. Wu, M. Magrakvelidze, L. Schmidt, M. Kunitski, T. Pfeifer, M. Schöffler, M. Pitzer, M. Richter, S. Voss, H. Sann, H. Kim, J. Lower, T. Jahnke, A. Czasch, U. Thumm, and R. Dörner, Understanding the role of phase in chemical bond breaking with coincidence angular streaking, *Nat. Commun.* **4**, 2177 (2013).
- [19] T.-Y. Xu and F. He, Dissociation of D_2^+ by UV and THz light pulses, *Phys. Rev. A* **88**, 043426 (2013).
- [20] H. Xu, T.-Y. Xu, F. He, D. Kielpinski, R. T. Sang, and I. V. Litvinyuk, Effect of nuclear mass on carrier-envelope-phase-controlled electron localization in dissociating molecules, *Phys. Rev. A* **89**, 041403 (2014).
- [21] H. Xu, H. Hu, X.-M. Tong, P. Liu, R. Li, R. T. Sang, and I. V. Litvinyuk, Coherent control of the dissociation probability of H_2^+ in ω - 3ω two-color fields, *Phys. Rev. A* **93**, 063416 (2016).
- [22] E. Lötstedt and K. Midorikawa, Laser-induced electron localization in a triatomic molecular ion, *Phys. Rev. A* **88**, 041402(R) (2013).
- [23] E. Lötstedt and K. Midorikawa, Carrier-envelope phase control of electron motion in laser-driven H_3^{2+} , *J. Phys. B* **47**, 204018 (2014).
- [24] G. J. Halász, A. Perveaux, B. Lasorne, M. A. Robb, F. Gatti, and Á. Vibók, Coherence revival during the attosecond electronic and nuclear quantum photodynamics of the ozone molecule, *Phys. Rev. A* **88**, 023425 (2013).
- [25] Y. Arasaki, K. Takatsuka, K. Wang, and V. McKoy, Time-resolved photoelectron spectroscopy of wavepackets through a conical intersection in NO_2 , *J. Chem. Phys.* **132**, 124307 (2010).
- [26] H. J. Wörner, J. B. Bertrand, B. Fabre, J. Higuier, H. Ruf, A. Dubrouil, S. Patchkovskii, M. Spanner, Y. Mairesse, V. Blanchet, E. Mével, E. Constant, P. B. Corkum, and D. M. Villeneuve, Conical intersection dynamics in NO_2 probed by homodyne high-harmonic spectroscopy, *Science* **334**, 208 (2011).
- [27] Y. Arasaki, Y. Mizuno, S. Scheit, and K. Takatsuka, Stark-assisted quantum confinement of wavepackets. A coupling of nonadiabatic interaction and CW-laser, *J. Chem. Phys.* **144**, 044107 (2016).
- [28] T. Szidarovszky and K. Yamanouchi, Photodissociation dynamics of weakly bound HeH_2^+ in intense light fields, *Phys. Rev. A* **94**, 063405 (2016).
- [29] G. Richings, I. Polyak, K. Spinlove, G. Worth, I. Burghardt, and B. Lasorne, Quantum dynamics simulations using Gaussian wavepackets: The vMCG method, *Int. Rev. Phys. Chem.* **34**, 269 (2015).
- [30] M. Vacher, M. J. Bearpark, and M. A. Robb, Direct methods for non-adiabatic dynamics: Connecting the single-set variational multi-configuration gaussian (vMCG) and Ehrenfest perspectives, *Theor. Chem. Acc.* **135**, 187 (2016).
- [31] M. Vacher, M. J. Bearpark, M. A. Robb, and J. P. Malhado, Electron Dynamics upon Ionization of Polyatomic Molecules: Coupling to Quantum Nuclear Motion and Decoherence, *Phys. Rev. Lett.* **118**, 083001 (2017).
- [32] M. Nest, The multi-configuration electron-nuclear dynamics method, *Chem. Phys. Lett.* **472**, 171 (2009).
- [33] P.-O. Löwdin, Quantum theory of many-particle systems. I. Physical interpretations by means of density matrices, natural spin-orbitals, and convergence problems in the method of configurational interaction, *Phys. Rev.* **97**, 1474 (1955).
- [34] T. Kato and K. Yamanouchi, Time-dependent multiconfiguration theory for describing molecular dynamics in diatomic-like molecules, *J. Chem. Phys.* **131**, 164118 (2009).

- [35] J. Zanghellini, M. Kitzler, C. Fabian, T. Brabec, and A. Scrinzi, An MCTDHF approach to multielectron dynamics in laser fields, *Laser Phys.* **13**, 1064 (2003).
- [36] T. Kato and H. Kono, Time-dependent multiconfiguration theory for electronic dynamics of molecules in an intense laser field, *Chem. Phys. Lett.* **392**, 533 (2004).
- [37] K. Ishikawa and T. Sato, A review on ab initio approaches for multielectron dynamics, *IEEE J. Sel. Topics Quantum Electron.* **21**, 1 (2015).
- [38] H.-D. Meyer, U. Manthe, and L. Cederbaum, The multi-configurational time-dependent Hartree approach, *Chem. Phys. Lett.* **165**, 73 (1990).
- [39] U. Manthe, H.-D. Meyer, and L. S. Cederbaum, Wave-packet dynamics within the multiconfiguration Hartree framework: General aspects and application to NOCl, *J. Chem. Phys.* **97**, 3199 (1992).
- [40] M. Beck, A. Jäckle, G. Worth, and H.-D. Meyer, The multiconfiguration time-dependent Hartree (MCTDH) method: A highly efficient algorithm for propagating wavepackets, *Phys. Rep.* **324**, 1 (2000).
- [41] H.-D. Meyer and G. A. Worth, Quantum molecular dynamics: Propagating wavepackets and density operators using the multiconfiguration time-dependent Hartree method, *Theor. Chem. Acc.* **109**, 251 (2003).
- [42] U. Manthe, Wavepacket dynamics and the multi-configurational time-dependent Hartree approach, *J. Phys.: Condens. Matter* **29**, 253001 (2017).
- [43] O. E. Alon, A. I. Streltsov, and L. S. Cederbaum, Multiconfigurational time-dependent Hartree method for bosons: Many-body dynamics of bosonic systems, *Phys. Rev. A* **77**, 033613 (2008).
- [44] O. E. Alon, A. I. Streltsov, and L. S. Cederbaum, Many-body theory for systems with particle conversion: Extending the multiconfigurational time-dependent Hartree method, *Phys. Rev. A* **79**, 022503 (2009).
- [45] L. Cao, S. Krönke, O. Vendrell, and P. Schmelcher, The multi-layer multi-configuration time-dependent Hartree method for bosons: Theory, implementation, and applications, *J. Chem. Phys.* **139**, 134103 (2013).
- [46] O. E. Alon, A. I. Streltsov, K. Sakmann, A. U. J. Lode, J. Grond, and L. S. Cederbaum, Recursive formulation of the multiconfigurational time-dependent Hartree method for fermions, bosons and mixtures thereof in terms of one-body density operators, *Chem. Phys.* **401**, 2 (2012).
- [47] L. Cao, V. Bolsinger, S. I. Mistakidis, G. M. Koutentakis, S. Krönke, J. M. Schurer, and P. Schmelcher, A unified ab initio approach to the correlated quantum dynamics of ultracold fermionic and bosonic mixtures, *J. Chem. Phys.* **147**, 044106 (2017).
- [48] Y. Ide, T. Kato, and K. Yamanouchi, Non-Born-Oppenheimer molecular wave functions of H_2 by extended multiconfiguration time-dependent Hartree-Fock method, *Chem. Phys. Lett.* **595-596**, 180 (2014).
- [49] T. Kato and K. Yamanouchi, Protonic structure of CH_3OH described by electroprotonic wave functions, *Phys. Rev. A* **85**, 034504 (2012).
- [50] I. S. Ulusoy and M. Nest, The multi-configuration electron-nuclear dynamics method applied to LiH, *J. Chem. Phys.* **136**, 054112 (2012).
- [51] D. J. Haxton, K. V. Lawler, and C. W. McCurdy, Multiconfiguration time-dependent Hartree-Fock treatment of electronic and nuclear dynamics in diatomic molecules, *Phys. Rev. A* **83**, 063416 (2011).
- [52] D. J. Haxton, K. V. Lawler, and C. W. McCurdy, Qualitative failure of a multiconfiguration method in prolate spheroidal coordinates in calculating dissociative photoionization of H_2^+ , *Phys. Rev. A* **91**, 062502 (2015).
- [53] C. Jhala and M. Lein, Multiconfiguration time-dependent Hartree approach for electron-nuclear correlation in strong laser fields, *Phys. Rev. A* **81**, 063421 (2010).
- [54] G. A. Worth, H.-D. Meyer, and L. S. Cederbaum, Relaxation of a system with a conical intersection coupled to a bath: A benchmark 24-dimensional wave packet study treating the environment explicitly, *J. Chem. Phys.* **109**, 3518 (1998).
- [55] M. Ehara, H.-D. Meyer, and L. S. Cederbaum, Multiconfiguration time-dependent Hartree (MCTDH) study on rotational and diffractive inelastic molecule-surface scattering, *J. Chem. Phys.* **105**, 8865 (1996).
- [56] Y. Ide, T. Kato, and K. Yamanouchi, Natural orbitals and potential curves within the framework of extended multiconfiguration time-dependent Hartree-Fock method, in *19th International Conference on Ultrafast Phenomena* (Optical Society of America, Okinawa, 2014), p. 07.Mon.P1.16.
- [57] R. T. Pack and G. A. Parker, Quantum reactive scattering in three dimensions using hyperspherical (APH) coordinates. Theory, *J. Chem. Phys.* **87**, 3888 (1987).
- [58] P. J. Mohr, D. B. Newell, and B. N. Taylor, CODATA recommended values of the fundamental physical constants: 2014, *J. Phys. Chem. Ref. Data* **45**, 043102 (2016).
- [59] P. A. M. Dirac, Note on exchange phenomena in the Thomas atom, *Math. Proc. Camb. Philos. Soc.* **26**, 376 (1930).
- [60] J. Frenkel, *Wave Mechanics, Advanced General Theory* (Oxford University Press, London, 1934).
- [61] P.-O. Löwdin and P. K. Mukherjee, Some comments on the time-dependent variation principle, *Chem. Phys. Lett.* **14**, 1 (1972).
- [62] H. Kono, Y. Sato, M. Kanno, K. Nakai, and T. Kato, Theoretical investigations of the electronic and nuclear dynamics of molecules in intense laser fields: Quantum mechanical wave packet approaches, *Bull. Chem. Soc. Jpn.* **79**, 196 (2006).
- [63] J. M. Taylor, Z.-C. Yan, A. Dalgarno, and J. F. Babb, Variational calculations on the hydrogen molecular ion, *Mol. Phys.* **97**, 25 (1999).
- [64] Y. Ning and Z.-C. Yan, Variational energy bounds for the hydrogen molecular ion, *Phys. Rev. A* **90**, 032516 (2014).
- [65] H. Nakashima, Y. Hijikata, and H. Nakatsuji, Solving the non-Born-Oppenheimer Schrödinger equation for the hydrogen molecular ion with the free complement method. II. Highly accurate electronic, vibrational, and rotational excited states, *Astrophys. J.* **770**, 144 (2013).
- [66] C. L. Beckel, B. D. Hansen III, and J. M. Peek, Theoretical study of H_2^+ ground electronic state spectroscopic properties, *J. Chem. Phys.* **53**, 3681 (1970).
- [67] A. Hanusch, J. Rapp, M. Brics, and D. Bauer, Time-dependent renormalized-natural-orbital theory applied to laser-driven H_2^+ , *Phys. Rev. A* **93**, 043414 (2016).
- [68] R. Anzaki, T. Sato, and K. L. Ishikawa, A fully general time-dependent multiconfiguration self-consistent-field method for

- the electron-nuclear dynamics, *Phys. Chem. Chem. Phys.* **19**, 22008 (2017).
- [69] B. C. Carlson and J. M. Keller, Eigenvalues of density matrices, *Phys. Rev.* **121**, 659 (1961).
- [70] I. Kawata, H. Kono, Y. Fujimura, and A. D. Bandrauk, Intense-laser-field-enhanced ionization of two-electron molecules: Role of ionic states as doorway states, *Phys. Rev. A* **62**, 031401(R) (2000).
- [71] Y. Sato, H. Kono, S. Koseki, and Y. Fujimura, Description of molecular dynamics in intense laser fields by the time-dependent adiabatic state approach: Application to simultaneous two-bond dissociation of CO₂ and its control, *J. Am. Chem. Soc.* **125**, 8019 (2003).
- [72] L. S. Cederbaum, Born-Oppenheimer approximation and beyond for time-dependent electronic processes, *J. Chem. Phys.* **128**, 124101 (2008).
- [73] M. Garg, A. K. Tiwari, and D. Mathur, Quantum dynamics of H₂⁺ in intense laser fields on time-dependent potential energy surfaces, *J. Phys. Chem. A* **116**, 8762 (2012).
- [74] D. Dey and A. K. Tiwari, Coupled electron-nuclear dynamics on H₂⁺ within time-dependent Born-Oppenheimer approximation, *J. Phys. Chem. A* **120**, 8259 (2016).
- [75] G. Hunter, Conditional probability amplitudes in wave mechanics, *Int. J. Quantum Chem.* **9**, 237 (1975).
- [76] A. Abedi, N. T. Maitra, and E. K. U. Gross, Exact Factorization of the Time-Dependent Electron-Nuclear Wave Function, *Phys. Rev. Lett.* **105**, 123002 (2010).
- [77] A. Abedi, N. T. Maitra, and E. K. U. Gross, Correlated electron-nuclear dynamics: Exact factorization of the molecular wavefunction, *J. Chem. Phys.* **137**, 22A530 (2012).
- [78] A. Abedi, F. Agostini, Y. Suzuki, and E. K. U. Gross, Dynamical Steps that Bridge Piecewise Adiabatic Shapes in the Exact Time-Dependent Potential Energy Surface, *Phys. Rev. Lett.* **110**, 263001 (2013).
- [79] J. L. Alonso, J. Clemente-Gallardo, P. Echenique-Robba, and J. A. Jover-Galtier, Comment on “Correlated electron-nuclear dynamics: Exact factorization of the molecular wavefunction” [*J. Chem. Phys.* **137**, 22A530 (2012)], *J. Chem. Phys.* **139**, 087101 (2013).
- [80] A. Abedi, N. T. Maitra, and E. K. U. Gross, Response to “Comment on ‘Correlated electron-nuclear dynamics: Exact factorization of the molecular wavefunction’” [*J. Chem. Phys.* **139**, 087101 (2013)], *J. Chem. Phys.* **139**, 087102 (2013).
- [81] Y. Suzuki, A. Abedi, N. T. Maitra, K. Yamashita, and E. K. U. Gross, Electronic Schrödinger equation with nonclassical nuclei, *Phys. Rev. A* **89**, 040501 (2014).
- [82] E. Khosravi, A. Abedi, and N. T. Maitra, Exact Potential Driving the Electron Dynamics in Enhanced Ionization of H₂⁺, *Phys. Rev. Lett.* **115**, 263002 (2015).
- [83] Y. Suzuki, A. Abedi, N. T. Maitra, and E. K. U. Gross, Laser-induced electron localization in H₂⁺: Mixed quantum-classical dynamics based on the exact time-dependent potential energy surface, *Phys. Chem. Chem. Phys.* **17**, 29271 (2015).
- [84] T. Kato, Y. Ide, and K. Yamanouchi, Molecular wave function and effective adiabatic potentials calculated by extended multi-configuration time-dependent Hartree-Fock method, in *International Conference of Computational Methods in Sciences and Engineering 2015 (ICCMSE 2015)*, AIP Conf. Proc. No. 1702, edited by T. E. Simos, Z. Kalogiratou, and T. Monovasilis (AIP, Melville, NY, 2015).
- [85] M. W. J. Bromley and B. D. Esry, Classical aspects of ultracold atom wave packet motion through microstructured waveguide bends, *Phys. Rev. A* **69**, 053620 (2004).
- [86] J. Caillat, J. Zanghellini, M. Kitzler, O. Koch, W. Kreuzer, and A. Scrinzi, Correlated multi-electron systems in strong laser fields: A multiconfiguration time-dependent Hartree-Fock approach, *Phys. Rev. A* **71**, 012712 (2005).
- [87] J. Crank and P. Nicolson, A practical method for numerical evaluation of solutions of partial differential equations of the heat-conduction type, *Proc. Camb. Philos. Soc.* **43**, 50 (1947), reprinted in *Adv. Comput. Math.* **6**, 207 (1996).
- [88] R. J. LeVeque, *Finite Difference Methods for Ordinary and Partial Differential Equations* (Society for Industrial and Applied Mathematics, Philadelphia, 2007).